The Astrophysical Journal, 810:97 (17pp), 2015 September 10 doi:10.1088/0004-637X/810/2/97

PARTICLE ACCELERATION AT LOW CORONAL COMPRESSION REGIONS AND SHOCKS

N. A. Schwadron[1], M. A. Lee[1], M Gorby[1], N. Lugaz[1], H. E. Spence[1], M. Desai[2], T. Török[3], C. Downs[3], J. Linker[3], R. Lionello[3], Z. Mikić[3], P. Riley[3], J. Giacalone[4], J. R. Jokipii[4], J. Kota[4], and K. Kozarev[5]
[1] University of New Hampshire, Durham, NH 03824, USA
[2] Southwest Research Institute, San Antonio, TX 78238, USA
[3] Predictive Science Inc., San Diego, CA 92121, USA
[4] University of Arizona, Tucson, AZ 85721, USA
[5] Harvard-Smithsonian Center for Astrophysics, Cambridge, MA 02138, USA
Received 2015 April 8; accepted 2015 August 4; published 2015 September 3

ABSTRACT

We present a study on particle acceleration in the low corona associated with the expansion and acceleration of coronal mass ejections (CMEs). Because CME expansion regions low in the corona are effective accelerators over a finite spatial region, we show that there is a rigidity regime where particles effectively diffuse away and escape from the acceleration sites using analytic solutions to the Parker transport equation. This leads to the formation of broken power-law distributions. Based on our analytic solutions, we find a natural ordering of the break energy and second power-law slope (above the break energy) as a function of the scattering characteristics. These relations provide testable predictions for the particle acceleration from low in the corona. Our initial analysis of solar energetic particle observations suggests a range of shock compression ratios and rigidity dependencies that give rise to the solar energetic particle (SEP) events studied. The wide range of characteristics inferred suggests competing mechanisms at work in SEP acceleration. Thus, CME expansion and acceleration in the low corona may naturally give rise to rapid particle acceleration and broken power-law distributions in large SEP events.

Key words: acceleration of particles – Sun: coronal mass ejections (CMEs) – Sun: flares – Sun: particle emission

1. INTRODUCTION

Large solar energetic particle (SEP) events are extremely dangerous to astronauts (Cucinotta et al. 2010; Schwadron et al. 2010) and electronic equipment in space. However, developing the ability to predict where and when SEPs will arise depends fundamentally on an understanding of the underlying physical mechanisms that control energetic particle acceleration and propagation.

Particle acceleration is believed to be associated with flare acceleration and the shocks driven by coronal mass ejections (CMEs; see a recent review by Aschwanden 2006). Recent research has highlighted the importance of CME development and associated particle acceleration low in the corona. For example, Gopalswamy et al. (2005) studied the CME heights at times of energetic particle release times. They found that particle acceleration typically began at heights from ~1.4 to 8.7 solar radii. This work is highly consistent with timing studies based on in situ observations showing that energetic particles are often accelerated as low as 2 solar radii (Reames 2009a, 2009b). Remote observations confirm that CME-driven shock waves occur low in the corona, typically below 2 solar radii (Liu et al. 2010; Veronig et al. 2010; Kozarev et al. 2011; Ma et al. 2011). However, the region between 1 and 10 solar radii remains extremely difficult to treat due to the complexity of the magnetic structure, the difficulty in understanding how CMEs are initiated, and how to treat the underlying particle acceleration. Theoretical estimates based on numerical MHD simulations and kinetic models (e.g., Kozarev et al. 2013) demonstrate that understanding of particle acceleration and accurately describing the formation of CMEs in the low corona pose significant challenges.

Simulations and theories of particle acceleration have confirmed that the low corona is an environment that supports the conditions necessary for particle acceleration to high energies. Particle-in-cell simulations of particle acceleration provide significant insight into the underlying physical mechanisms associated with shock acceleration (Giacalone 2005). However, global shock acceleration and particle propagation models often focus on interplanetary space between ~20 solar radii and 1 astronomical unit (AU), where shocks become very strong and create hazardous gradual radiation events (Verkhoglyadova et al. 2008; Zhang et al. 2009). Sophisticated simulations of CMEs and related shocks have shown that diffusive shock acceleration is capable of accelerating solar energetic protons up to very high energies of 10 GeV for very strong shocks (Tsurutani et al. 2003; Roussev et al. 2004; Kocharov et al. 2005; Manchester et al. 2005).

Recently, Schwadron et al. (2014) showed the first results of the application of the Energetic Particle Radiation Environment Model (EPREM; Schwadron et al. 2010) for describing particle acceleration arising from a modeled CME low in the corona. The modeling represents a combination of an energetic particle solver that describes the evolution of the particle distribution based on the focused transport equation and simulated MHD fields. EPREM uses a methodology for energetic particle modeling based on a concept first introduced by Kóta et al. (2005a, 2005b) that utilizes a Lagrangian system co-moving with the plasma for the energetic particle transport equation. The same approach was used by Kozarev et al. (2013) to describe particle acceleration from the low corona during CME acceleration. In this case, the acceleration of the CME was modeled with the Michigan Block-Adaptive-Tree-Solarwind-Roe-Upwind-Scheme MHD code and coupled with the kinetic energetic particle model (EPREM) to characterize the acceleration of energetic particles.

The MHD fields used by Schwadron et al. (2014) are solved for using a coupled set of models, Corona–Heliosphere (CORHEL) for the ambient solar corona, solar wind (Lionello

et al. 2009; Riley & Lionello 2011; Riley et al. 2012), and CMEs. CORHEL utilizes the Magnetohydrodynamic Algorithm outside a Sphere (MAS) code (e.g., Mikić & Linker 1994; Lionello et al. 1999; Mikić et al. 1999) that advances the standard viscous and resistive MHD equations in spherical coordinates. The model incorporates radiative losses, thermal conduction parallel to the magnetic field, and an empirical coronal heating function.

Generally, large amounts of particle acceleration occurring low in the corona after fast expansion of a CME can be traced back to the formation of large-scale compression regions and shocks near the legs of the CME (Gorby et al. 2012; Linker et al. 2014; Schwadron et al. 2014). In both the case of particle acceleration in compression regions (see Giacalone et al. 2002; Jokipii et al. 2003) and at shocks (e.g., Fermi 1949; Drury 1983), particles can move back and forth across the structure to gain energy after each crossing of the plasma gradient or shock. In the case of shocks, the net energy gain depends on the number of shock crossings (Bell 1978a, 1978b). Diffusive acceleration generally requires a short scattering mean free path (Lee et al. 1981; Lee 1983, 2005) or a quasi-perpendicular configuration for efficient particle acceleration (Jokipii 1982, 1986, 1987). These conditions allow for a high rate of crossings of the speed gradient, and therefore lead to a high rate of particle acceleration.

Another important observational factor in the development of our understanding of large SEP events (particularly ground-level events) is the common occurrence of broken power-law distributions (Mason et al. 2002; Mewaldt et al. 2005a, 2005b, 2012). Recent work (Desai et al. 2015) has shown that the power-law break has a rigidity dependence that suggests strong wave–particle interactions.

The physical mechanisms resulting in these broken power laws are still unknown. In this paper, we show that broken power-law distributions could result from size-limited shocks or compressions in the low corona. We then detail the types of composition signatures that would be expected from particle acceleration that occurs in these structures.

The methodology used here follows from an analytic solution of the Parker transport equation in the presence of size-limited acceleration regions. The approach, while simple, provides significant insight into the underlying physics that leads to particle acceleration to high energies and the formation of broken power-law distributions from the low corona. In particular, this work aids in the interpretation of numerical solutions from EPREM and other numerical models.

A second central question addressed in this work is what types of energetic particle signatures do we expect from low coronal shocks and compressions? In this paper, we begin to develop an analytic framework to answer that question. This analytic framework is important not only in allowing for interpretation of observational results, but also for understanding the implications of detailed numerical simulations of CMEs for particle acceleration.

The paper is organized as follows. Section 2 discusses the basic theory of size-limited shocks or compressions in the low corona. Section 3 discusses observational implications of the size-limited acceleration regions from the low corona. Section 4 ends the paper with discussion and conclusions.

The appendices detail results used in the paper for modeling of CMEs in the low corona (detailed in Appendix A) and theoretical treatments of energetic particle injection and acceleration. The energetic particle treatments are detailed in a series of appendices: Appendix B describes the scattering mean paths in the low corona associated with parallel and perpendicular diffusion; Appendix C discusses the injection of particles into the diffusive acceleration process; Appendix D provides the analytical solution to diffusive acceleration at a size-limited shock or acceleration region.

The analytic solution is broken into several components: Appendix D.1 explores the analytic solution for injection at an individual location along the shock or compression where the spatial dependence is considered only within the coplanarity plane (containing the magnetic field); Appendix D.2 then explores the corresponding solution where the spatial dependence is considered only out of the plane of coplanarity; Appendix D.3 generalizes the results of the previous two subsections for 3D motion and diffusion along the shock or compression; Appendix D.4 then solves for the distribution function for injection taken as an integrated region along the shock or compression; Appendix D.5 shows how loss processes can be accounted for in these solutions.

2. DIFFUSIVE PARTICLE ACCELERATION AT LOW CORONAL SHOCKS AND COMPRESSIONS: PARTICLE ACCELERATION ON SIZE-LIMITED FRONTS

Our analysis is motivated by recent results of a simulation of a CME formed low in the corona using the MAS model developed by Predictive Science. Appendix A details the configuration used for the simulation. The simulation revealed a CME that rapidly accelerated low in the corona, causing extremely strong compression regions to form close to the Sun (Figure 1 of Schwadron et al. 2014).

We consider the configuration shown in Figure 1 where a shock or compression region driven by a CME expansion creates the conditions for diffusive shock acceleration low in the corona. Often a description of diffusive acceleration at shocks is solved for using as a starting point the Parker transport equation:

$$\frac{\partial f}{\partial t} + \boldsymbol{u}\cdot\nabla f - \nabla\cdot(\mathsf{K}\cdot\nabla f) - \frac{\nabla\cdot\boldsymbol{u}}{3}p\frac{\partial f}{\partial p} = Q_0\delta(x)\delta(z)\delta(p - p_{\rm inj}), \quad (1)$$

where

$$\mathsf{K} = \kappa_{\parallel}\hat{e}_b\hat{e}_b + \kappa_{\perp}(\mathsf{I} - \hat{e}_b\hat{e}_b) \quad (2)$$

and $\kappa_{\parallel}$ and $\kappa_{\perp}$ are the diffusion coefficients parallel and perpendicular to the magnetic field, respectively. The form of the diffusion tensor indicated here is diagonal.

An off-diagonal term, $\kappa_{\rm A}$, due to drift is sometimes included in the diffusion tensor. Alternatively, an explicit drift term, $\nabla\cdot[cvp\boldsymbol{B}/(3qB^2)\times\nabla f]$, may be included on the left-hand side of the Parker equation. Drift leads to motion out of the coplanarity plane, which is detailed in Appendix D.2. Generally, the effect of motion out of the coplanarity plane is small, except for shocks or compressions with obliquity angles very close to 90°. While neglected here, largely for simplicity, we emphasize that this term may need to be accounted for in future studies that examine large events from highly oblique shocks and compressions.

The source term, which is also detailed in Appendix D.1, is a slight modification of the standard treatment for

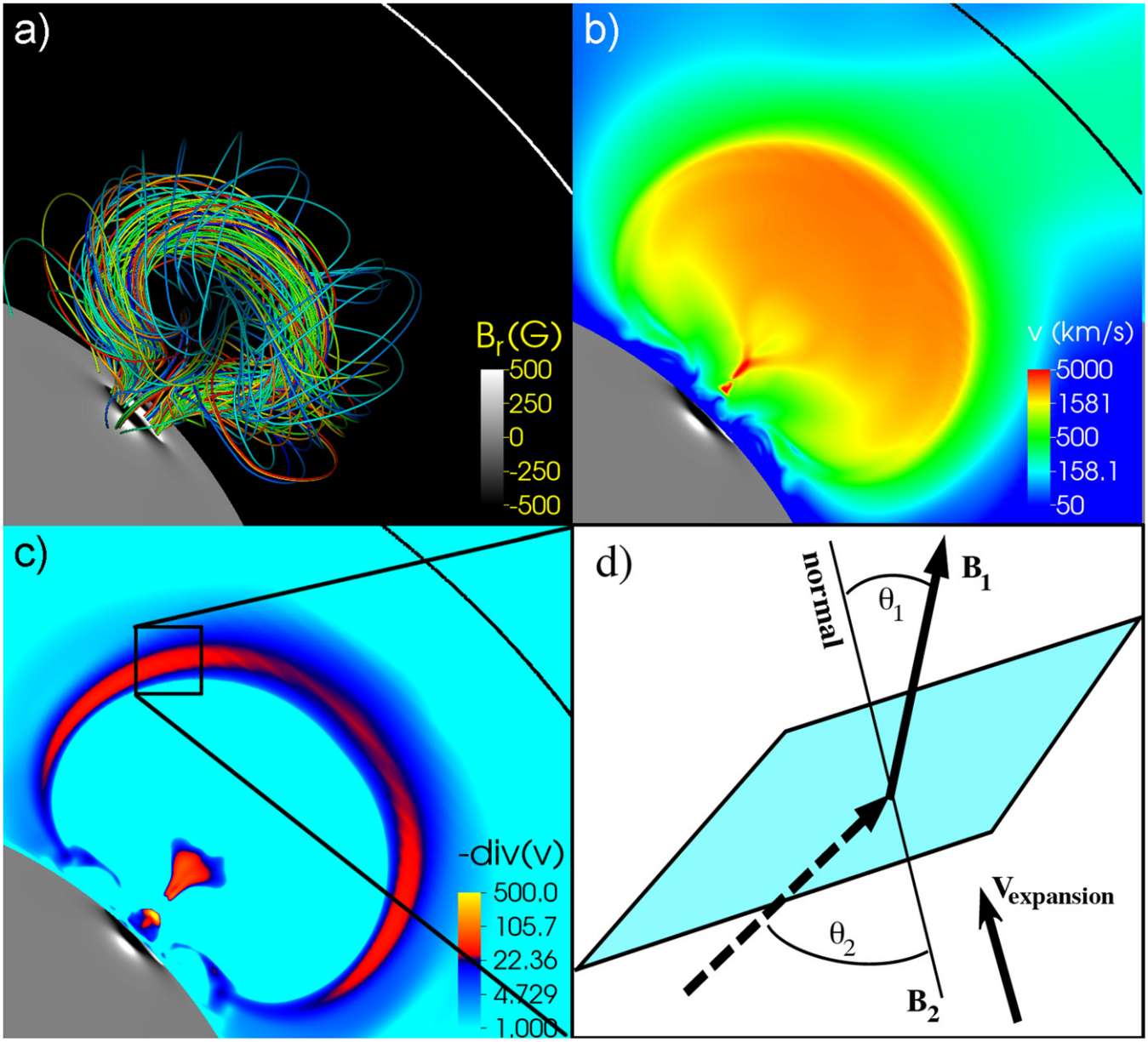

Figure 1. Configuration in the low corona based on MAS simulations (Schwadron et al. 2014) showing a strong compression driven by the expansion of a CME. The strong compressions on the flank of the CME create the conditions that lead to rapid particle acceleration. The configuration of the erupting magnetic flux rope (panel (a)) is shown with associated photospheric field strength B_r in grayscale on the solar surface. The CME accelerates rapidly to plasma speeds (panel (b)) of thousands of km s^{-1} low in the corona. As a result of the CME's rapid acceleration, strong compressions and shocks are formed showing a large negative velocity divergence, $\nabla \cdot \boldsymbol{u}$ (panel (c)) expressed in code units corresponding to 7×10^{-4} s^{-1}. The box in panel (c) is blown out (panel (d)) to indicate the plane of the shock or compression and a magnetic flux bundle piercing the shock. In panel (d), note the magnetic field normal angles θ_1 and θ_2 upstream and downstream from the shock or compression. The expansion velocity driving these compressions is also shown.

diffusive shock acceleration theory, in which particles are injected at a fixed energy and at the shock ($x = 0$). Here, the shock or compression is within a plane ($y - z$) centered at $x = 0$. Magnetic field lines lie within the $x - z$ plane (coplanarity). Particles are injected at a fixed location ($z = 0$) in the coplanarity plane. This same concept was introduced by Schwadron et al. (2008) to model particle acceleration at the blunt termination shock. We first solve for a Green's function for injection at a fixed location along the shock, at $z = 0$, and then integrate over the region along the shock, from $z = 0$ to $z = L$, in which particles are injected. The constant Q_0 in the source term scales the injection of particles,

$$Q_0 = u_1 \epsilon \, f_{\rm inj} L p_{\rm inj}, \tag{3}$$

where ϵ is the injection efficiency, $f_{\rm inj}$ is the distribution function at the injection energy, and L is size-scale of the shock.

As shown in Figure 2, we track the quantity $\nabla \cdot \boldsymbol{V}$ in the MAS code along a magnetic flux bundle on the flanks of the expanding CME. We observe that the acceleration region is most pronounced where the CME expansion and acceleration is strongest. On the flux bundle shown here, the outward speed of the CME expansion is $<$600 km s^{-1} at 1.5 solar radii. By the

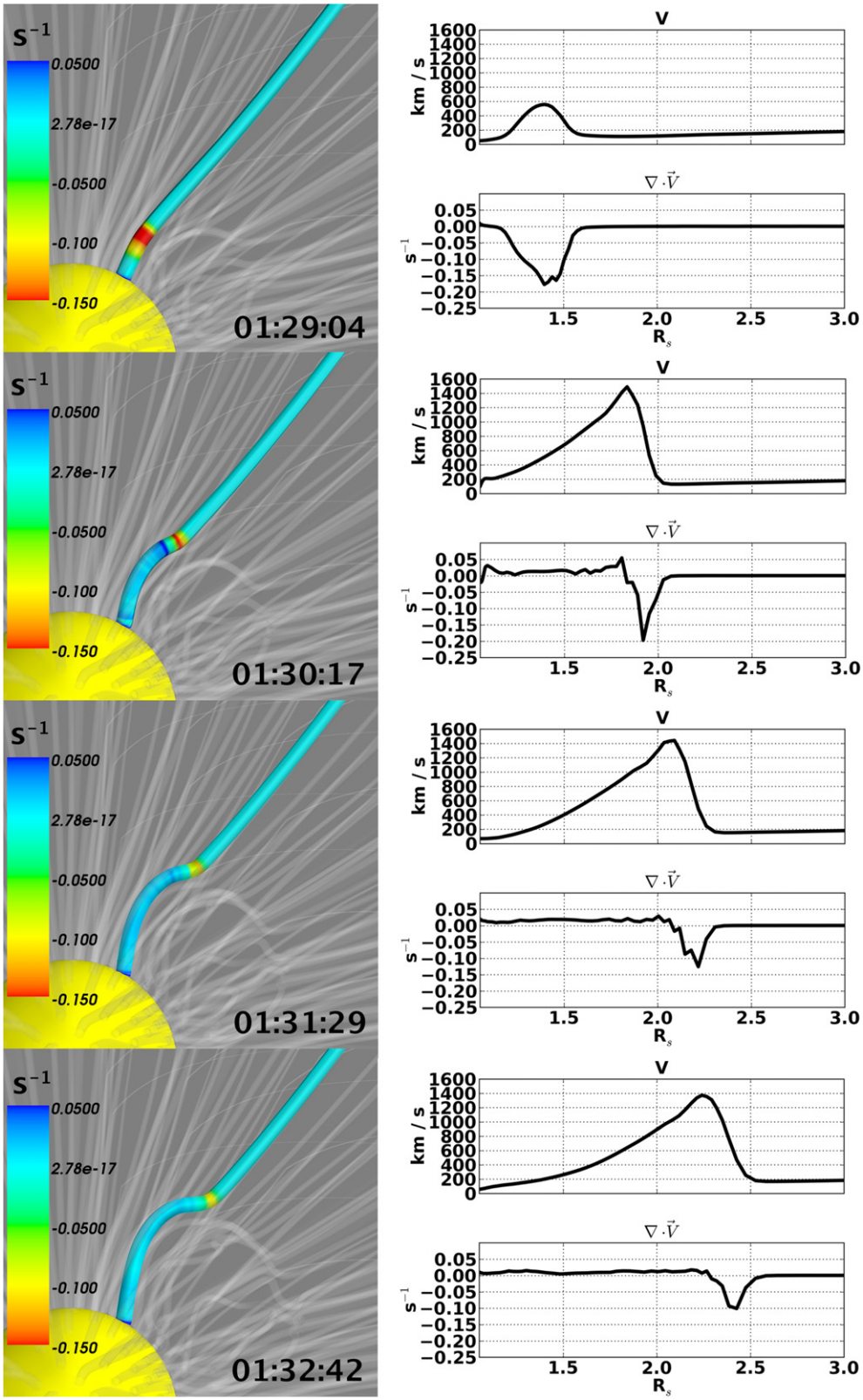

Figure 2. We show the development of a compression region on a bundle of field lines. The curves on the right show V and $\nabla \cdot \boldsymbol{V}$ along the field line bundle as the CME expansion acts in the low corona at four different instances within the simulation. The configuration on the left shows the open magnetic field bundle (depicted as a tube) that is deformed by the expansion of the CME. The color-coding on this field line bundle indicates $\nabla \cdot \boldsymbol{V}$. Times are in hh:mm:ss, where time zero corresponds to $t = 182\tau_A$ (see Appendix A). Note that the simulation shows the formation of a coronal compression region low in the corona, causing $|\nabla \cdot \boldsymbol{V}|$ to increase. After the initial expansion, $|\nabla \cdot \boldsymbol{V}|$ forms a maximum and then falls at later times as the CME pushes the compressed sheath into the inner heliosphere.

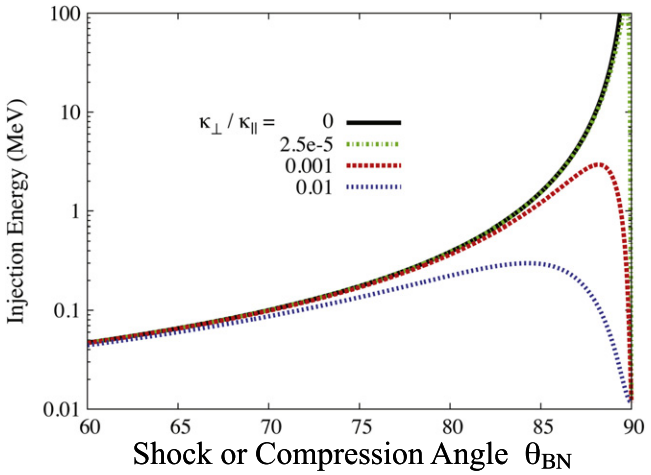

Figure 3. Injection energy (in MeV) for particles with a range of different levels of perpendicular diffusion ($\kappa_\perp/\kappa_\parallel$) and at a range of different shock angles (the angle between the shock normal and the magnetic field).

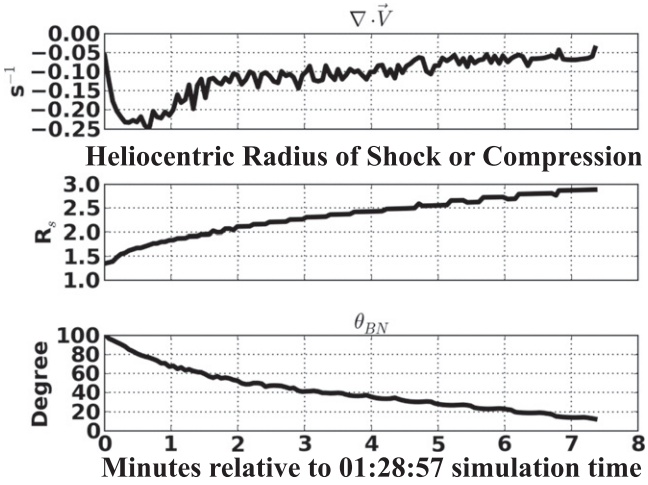

Figure 4. Utilizing the flux bundle tracked in Figure 2, we find the velocity divergence (top panel), shock or compression radius (middle panel), and θ_{BN} (magnetic field angle with respect to the shock normal). The time axis is relative to 01:28:57 in the simulation time.

time this expansion reaches 1.8 solar radii, the expansion speed reaches $\sim$1500 km s^{-1}. After this point, the acceleration of the CME slows, and the speed of the CME expansion roughly levels off at around 1400 km s^{-1}.

In the right panels of Figure 2, we include the divergence of the plasma velocity. This divergence provides an excellent indicator for the pronounced effects of the CME expansion and acceleration. The divergence is largest between 1.5 and 2 solar radii and then falls off at larger distances.

The fourth term on the left-hand side of the Parker transport Equation (1) includes the divergence in the plasma velocity. It is precisely this term that leads to the acceleration of energetic particles. Because the CME acceleration is prompt and roughly localized between 1.5 and 2 solar radii, this is also the location where we expect prompt acceleration of energetic particles.

The localization of the acceleration region motivates a treatment of the shock acceleration process detailed in Appendix D.4. One of the important features of the configuration of the acceleration region is that the connection between the shock or compression and a magnetic field line (or flux bundle) moves along the structure. This motion of this connection point occurs as particles are being accelerated. Therefore, on average, the higher the energy of the particle distribution, the longer the flux bundle near which these particles are accelerated has remained in contact with the shock or compression. Because of the finite size of the shock or compression, a flux bundle connection point eventually moves off of the accelerator, which then limits the maximum energy gain of the particles and, as we will show, leads to the formation of a broken power-law in the particle distribution.

The diffusive acceleration process starts at a specific energy, the injection energy, which is quantified in Appendix C and shown in Figure 3 as a function of $\kappa_\perp/\kappa_\parallel$ at a fixed obliquity. The rate of acceleration is strongly influenced by the obliquity of the shock or compression and the diffusion coefficient. The parallel diffusion coefficient is given as $\kappa = v\lambda_\parallel/3$, where $\lambda_\parallel$ is the parallel mean free path associated with particle scattering. As detailed in Appendix B, we have taken a scattering mean free path that scales as $\lambda_\parallel = \lambda_{\parallel 0}(R_g/R_{g0})^\chi$, where $R_g = pc/q$ is the particle rigidity and $R_{g0} = (m_p v_0 c/e)(A_0/Z_0)$ is a reference rigidity at mass $m_0 = A_0 m_p$, charge $q_0 = Z_0 e$, and speed v_0.

The simulation analyzed here allows us to investigate the angle between the shock normal and the magnetic field (θ_{BN}). In principle, the rapid expansion of the CME should result in a quasi-perpendicular shock or compression close to the Sun. Figure 4 demonstrates the transition of the shock or compression from a quasi-perpendicular structure close the Sun ($<2R_s$) to a quasi-parallel structure farther out ($>2.5R_s$). The figure also shows that the shock or compression is quasi-perpendicular where the magnitude of divergence in velocity is largest.

Li et al. (2009) studied the rigidity dependence of wave–particle interactions at shocks of varying obliquities. Quasi-perpendicular shocks typically result in weak rigidity dependence ($\chi < 1$), whereas quasi-parallel shocks result in more pronounced rigidity dependence ($\chi > 1$). For reference speed v_0, we use a value consistent with a kinetic energy $T_0 = 1$ MeV/nuc.

Typical scattering mean free paths at 1 AU and MV rigidities scale from 0.01 to 1 AU (Dröge 2005). We adopt a 1 AU mean free path of 0.14 AU and use a $1/B$ scaling into the low corona. Assuming a typical 1 G field, we find a reference scattering mean free path of $\lambda_{\parallel 0} = 0.015$ R_s at $T_0 = 1$ MeV/nuc.

In this problem, acceleration time is an important factor. The acceleration rate (see Appendix D) is given by

$$d\tau_p = \frac{3\delta x}{\Delta u}\frac{dp}{p}, \tag{4}$$

where the characteristic width of the acceleration region is

$$\delta x = \frac{\kappa_{xx1}}{u_{x1}} + \frac{\kappa_{xx2}}{u_{x2}}. \tag{5}$$

Here, the component diffusion coefficients are

$$\kappa_{xx} = \kappa_\parallel \cos^2\theta + \kappa_\perp \sin^2\theta, \tag{6}$$

$$\kappa_{xz} = (\kappa_\parallel - \kappa_\perp)\sin\theta\cos\theta, \tag{7}$$

$$\kappa_{zz} = \kappa_\parallel \sin^2\theta + \kappa_\perp \cos^2\theta, \tag{8}$$

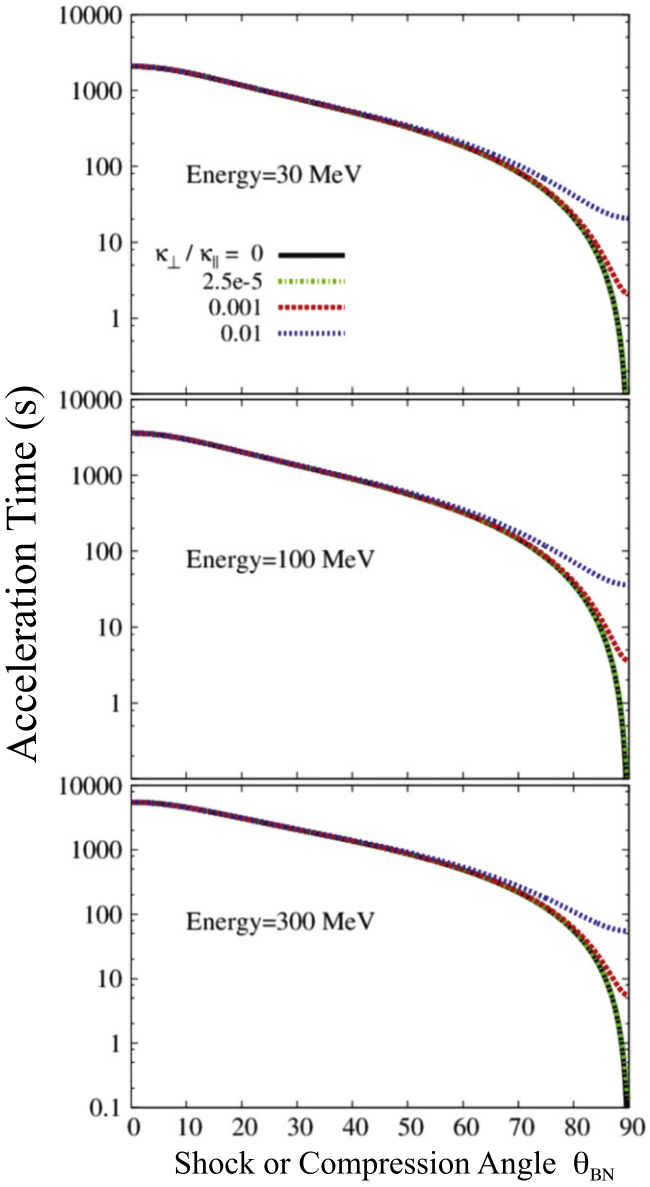

Figure 5. Acceleration time to the indicated energies as a function of the shock-normal angle with respect to the magnetic field. Small angles represent quasi-parallel configurations, whereas large angles represent quasi-perpendicular configurations. We have taken a compression ratio of 3. Prompt acceleration (on the scale of minutes) to high energies (>30 MeV) requires a quasi-perpendicular configuration.

and θ is the angle between the magnetic field and plasma flow. The acceleration time to a given momentum p is

$$\tau_p \approx \frac{3\delta x}{\Delta u} = \frac{d\tau_p}{d\,\ln p}. \tag{9}$$

Figure 5 shows the acceleration time as a function of the shock-normal angle with respect to the magnetic field. Small angles represent quasi-parallel configurations, whereas large angles represent quasi-perpendicular configurations. We have taken a compression ratio of 3. Note that for a quasi-perpendicular configuration (>70°) the acceleration time up to 100 MeV is on the order of minutes or less. Therefore, prompt acceleration to high energies in strong compression regions and shocks requires a quasi-perpendicular configuration.

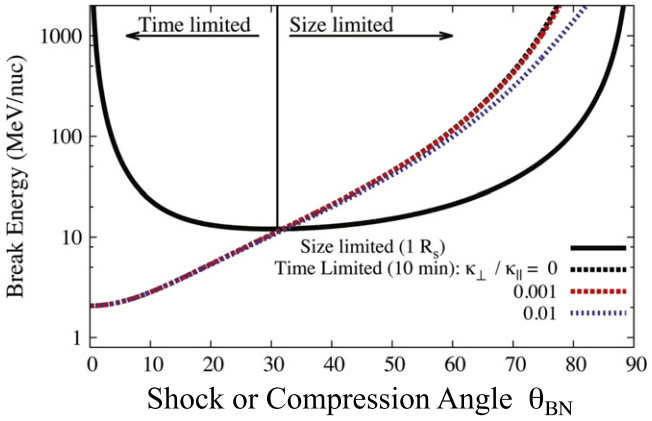

Figure 6. Break energy of accelerated particles as a function of the shock angle (field-flow angle). Size-limited break energies apply for large shock angles (>30°), whereas time-limited break energies apply for lower shock angles (<30°). Larger shock angles lead to higher break energies.

As detailed in Appendix D.1, the distance associated with motion along the shock in the coplanarity plane is

$$z_d = -\frac{3}{(\chi+1)\Delta u}(\kappa_{xz1} + \kappa_{xz2}), \tag{10}$$

where we have taken the flow normal to the shock, the diffusion coefficient is $\kappa_{xzi} = (\kappa_\parallel - \kappa_\perp)\sin\theta_i \cos\theta_i$, and the subscript i refers to upstream ($i = 1$) or downstream conditions ($i = 2$). We take a given shock length L as the region over which acceleration can occur. Utilizing Equation (10), we then derive the characteristic energy (per nucleon A) to which particles may be accelerated,

$$\frac{T_L}{A} \approx \frac{T_0}{A_0}\left(\frac{A_0 Z}{A Z_0}\right)^{2\chi/(\chi+1)} \times \left[|\chi+1|\,\frac{\Delta u}{v_0}\frac{2L}{3\lambda_{\parallel 0}}\left(1 - \kappa_\perp/\kappa_\parallel\right)^{-1} \times \left(\sin\theta_1\cos\theta_1 + \sin\theta_2\cos\theta_2\right)^{-1}\right]^{2/(\chi+1)}, \tag{11}$$

where $T_0 = m_0 v_0^2/2$. Note that the kinetic energy per nucleon scales as $T_L/A \propto (Z/A)^{2\chi/(\chi+1)}$. In the case where $\chi \approx 0$, the maximum energy does not depend on Z/A.

An alternative expression for the maximum characteristic energy makes use of the acceleration time, τ_p,

$$\frac{T_\tau}{A} \approx \frac{T_0}{A_0}\left(\frac{A_0 Z}{A Z_0}\right)^{2\chi/(\chi+1)}\left(\frac{\Delta u \tau_p}{\lambda_{\parallel 0}}\right)^{2/(\chi+1)} \times \left(v_0\left[\sum_{j=1}^{2}\frac{\cos^2\theta_j + (\kappa_\perp/\kappa_\parallel)\sin^2\theta_j}{u_{xj}}\right]\right)^{-2/(\chi+1)}. \tag{12}$$

Figure 6 shows these energy limits as a function of the shock angle. We refer to the limits as the break energy since particle distributions drop rapidly above the limit. We have assumed a size-scale of $L = 1\ R_s$ and an acceleration time of $\tau_p = 10$ minutes. At large shock angles (>30°), the characteristic size (L) of the accelerator presents the most significant limit on the energy of particles from the site of acceleration. At small shock angles (<30°), the characteristic time (τ_p) of the acceleration

presents the most significant limit on the break energy. Generally, larger shock angles lead to higher break energies.

Appendix D.4 considers injection along a shock of length L in the plane of the magnetic field (plane of coplanarity). For a fixed shock angle, we obtain the following solution:

$$F_L(z,p) = \frac{3u_1}{2\Delta u} f_{\rm inj}\,\epsilon \left(\frac{p}{p_{\rm inj}}\right)^{-\gamma} \times \left[\mathrm{erf}\left(\frac{L+z_d+z}{2\sqrt{D_z}}\right) - \mathrm{erf}\left(\frac{z_d+z}{2\sqrt{D_z}}\right)\right], \quad (13)$$

where

$$D_z = \frac{3}{2(\chi+1)\Delta u}\sum_{j=1}^{2}\left\{\frac{\kappa_{\parallel}\kappa_{\perp}}{u_{xj}} + \frac{(\kappa_{xzj})^2}{u_{xj}}\right\}. \quad (14)$$

Based on Kozarev et al. (2013) and Dayeh et al. (2009), we assume a population for the seed population with differential flux that scales as

$$J_{\rm seed}(T,r) = J_0\left(\frac{r_1}{r}\right)^2\left(\frac{T}{T_0}\right)^{-\gamma_s} \times \exp\left(-T/T_0\right), \quad (15)$$

where T is kinetic energy, $T_0 = 1$ MeV, $\gamma_s = 1.96$, and $J_0 = 7$ protons cm^{-2} s^{-1} sr $-$ 1 MeV $-$ 1. This injected spectrum is then converted into a distribution function to solve for $f_{\rm inj}$.

The solution for the distribution function stated above ignores the escape of particles from the shock. This is an important factor that helps to steepen the spectrum above the break energy. A solution that incorporates escape is developed in Appendix D.5:

$$F_L^{\rm escape}(z,p) = F_L(z,p)\,g^{\rm escape}(p), \quad (16)$$

where $F_L(z,p)$ is the previous total distribution with no loss effects, Equation (75), and the factor $g^{\rm loss}(p)$ is

$$g^{\rm escape}(p) \approx \exp\left(-\frac{6}{(\chi+1)\Delta u}\sum_{j=1}^{2}\sqrt{\frac{\kappa_{xxj}}{\tau}} \times \left[1 - \left(\frac{v_{\rm inj}}{v}\right)^{(\chi+1)/2}\right]\right) \quad (17)$$

and $v_{\rm inj}$ is the particle injection speed.

Figure 7 shows differential spectra that incorporate escape (Equation (16)) for several values of χ using a shock obliquity angle of 70°. Note the existence of both a spectral break and a roll-over at higher energies. The spectral break drops with energy for increasing values of χ. For comparison, Figure 8 shows the spectrum in the case in which there is no escape of particles from the shock accelerator.

The spectral break is associated with injection of particles along a fixed length L along the shock. Below the break energy, the spectrum attains a power law close to the result from steady diffusive acceleration. Above the break energy, the convection of the flux bundle through the injection region coupled with diffusion on and across the flux bundle away from the injection site causes the power law to steepen.

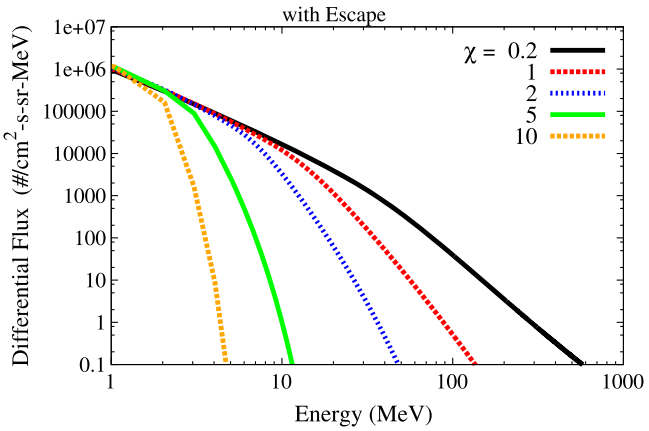

Figure 7. Differential spectra for several cases of χ based on Equation (16). This spectrum is developed for the case in which escape of particles from the shock is incorporated. Note the existence of a spectral break and a roll-over at higher energies. The spectral break drops with energy for increasing values of χ. These spectra are formed at $r \sim 1.5\ R_s$.

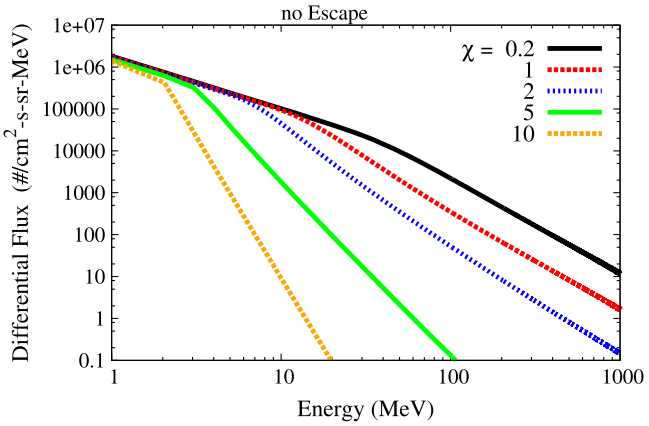

Figure 8. Differential spectra for several cases of χ based on Equation (75). In this case, loss of particles from the shock is neglected. Note the spectral break and the relatively smooth power law at higher energies. The spectral break drops with energy for increasing values of χ. These spectra are formed at $r \sim 1.5\ R_s$.

The spectra simulated by the model are fit to the same spectral form as used by Mewaldt et al. (2012):

$$J = CE^{\gamma_1}\exp\left(-E/E_0\right) \text{ for } E \leqslant (\gamma_1-\gamma_2)E_0 = CE^{\gamma_2}\left\{\left[(\gamma_1-\gamma_2)E_0\right]^{(\gamma_2-\gamma_1)}\exp(\gamma_2-\gamma_1)\right\}, \quad (18)$$

where we refer to E_0 as the break energy, γ_1 as the lower-energy power-law exponent, and γ_2 the higher-energy power-law exponent. Figure 9 shows the break energy as a function of the power-law exponent χ in rigidity ($\lambda_{\parallel} \propto R_g^{\chi}$) for three different size shocks and with and without escape from the shock. In all cases, we assume a driver speed of $u_1 \sim 1500$ km s^{-1}, a compression ratio at the shock of $r_c = 3$, and $\kappa_{\perp}/\kappa_{\parallel} = 0.001$. In addition to the simulations shown in these figures, we have explored the behavior of the solution for the distribution function. We observe that the break energy increases with the size of the shock, the CME driver speed, and with reductions in the scattering mean free path.

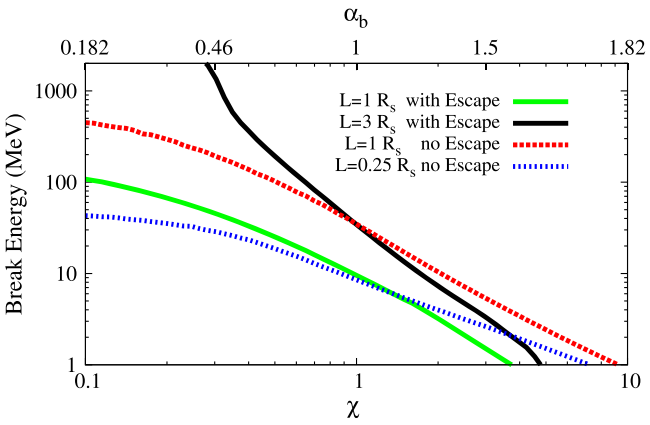

Figure 9. Break energy as a function of χ for three different size injection regions with and without escape of particles from the shock incorporated. The break energy increases with the size of the injection region. The break energy is also larger when loss from the shock is neglected. All curves all apply for $\lambda_{\|0} = 0.015\ R_s$. While the lower x-axis shows the break energy as a function of rigidity-dependent power-law exponent χ, the upper x-axis shows the corresponding charge-per-mass power-law exponent, α_b.

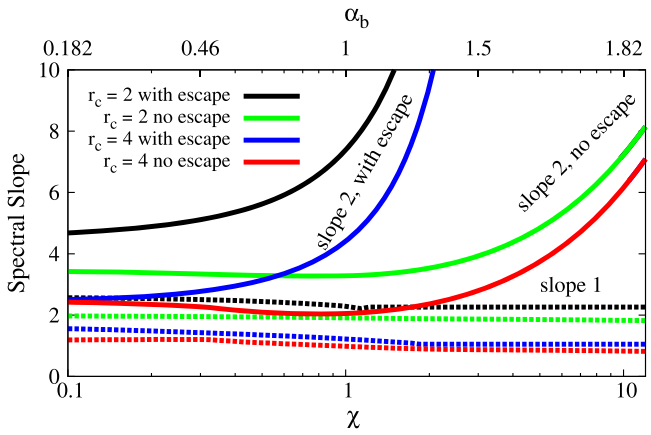

Figure 10. Slopes of the differential energy flux below (slope 1) and above (slope 2) the energy break for two different values of the compression ratio and situations where we include and neglect escape. Note that slope 1 is consistent with the results of diffusive shock acceleration theory, while slope 2 is steeper. Slope 2 increases sharply with χ and with α_b.

3. OBSERVATIONAL IMPLICATIONS OF SIZE-LIMITED PARTICLE ACCELERATION

In this section, we discuss observational implications of size-limited acceleration regions from the low corona based on the strong χ dependence of the break energy. Observationally, the rigidity dependence of the scattering appears most prominently in the mass-per-charge dependence of the break energy. Specifically, the break energy is plotted as a function of Z/A, and a power law is observed (Desai et al. 2015):

$$\frac{T_{\rm break}}{A} \propto \left(\frac{Z}{A}\right)^{\alpha_b}, \tag{19}$$

where the quantity α_b can be derived observationally. From Equations (11) and (19), we find that the power law is α_b, which is directly related to χ:

$$\alpha_b = 2\chi/(\chi + 1). \tag{20}$$

Note that χ is a positive quantity. From (20), we find that α_b should span the range $0 \leqslant \alpha_b < 2$.

A second feature demonstrated in Figure 9 is that the break energy decreases strongly with α_b. Increasing Z/A results in larger scattering mean free paths, and therefore less efficient acceleration.

We calculate the spectral slopes of the differential energy flux at energies below the break energy (slope 1, γ_1) and at energies above the break energy (slope 2, γ_2). Results are shown in Figure 10. The lower-energy spectral slope γ_1 is roughly consistent with results of diffusive shock acceleration,

$$\gamma_1 \approx \frac{r_c + 2}{2(r_c - 1)}. \tag{21}$$

The higher-energy spectral slope γ_2 is much steeper than γ_1, and γ_2 increases with χ and with α_b. When escape is included, the γ_2 steepens further.

Figure 11 shows observed spectral slopes from 16 ground-level events studied by Mewaldt et al. (2012). Note that the typical range of the lower-energy spectral slope is $\sim 1 - 2$. This suggests compression ratios in the range of 2–4 with an average compression ratio of $\sim$3.1.

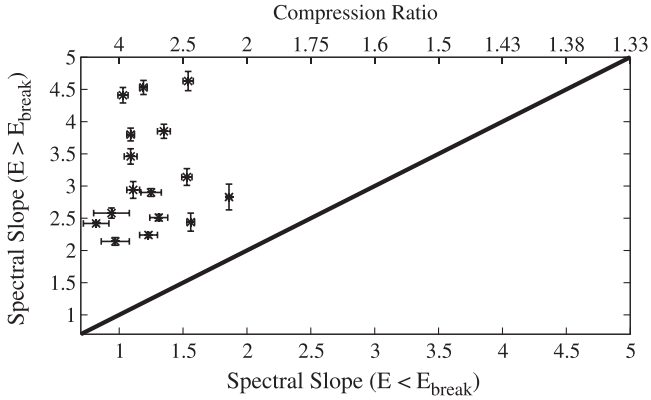

Figure 11. Observed spectral slopes associated with ground-level events from Mewaldt et al. (2012). The upper x-axis shows the compression ratio associated with shocks that produce a given value of the lower-energy spectral slope.

There are essentially no cases of low-energy spectral slopes that exceed 2.5. This suggests a lower limit for the compression ratio of $r_c = 1.75$. We may be observing a natural selection effect where weak shocks fail to produce sizable SEP events, and are therefore excluded from the data set.

The higher-energy spectral slope has an average $\gamma_2 \sim 3.2$ and a typical range 2.1–4.6. Based on the results in Figure 10, this range appears to be consistent with values of $\chi \sim 0.1 - 7$ ($\alpha_b \sim 0.2 - 1.75$) for cases in which escape is neglected and values of $\chi \sim 0.1 - 1$ ($\alpha_b \sim 0.2 - 1$) for cases in which escape is included. The mean value for the spectral slope ($\gamma_2 \sim 3.15$) appears roughly consistent with values of $\chi < 3$ and $\alpha_b < 1.5$ for cases in which escape is neglected or values of $\chi < 0.7$ and $\alpha_b < 0.6$ when a relatively weak shock ($r_c = 2$) is considered. The fact that slope 2 steepens sharply for $\chi > 1$ and $\alpha_b > 1$ when escape is included suggests that large quasi-perpendicular shocks ($\chi < 1$) have much harder spectra above the break energy as compared to quasi-parallel shocks ($\chi > 1$).

Figure 12 shows the break energy as a function of the difference between spectral slopes. Generally, for the range of injection regions considered and the conditions with and without escape, the predictions appear to roughly span the range of observations. To account for large break energies accompanied by large spectral slope differences, we must

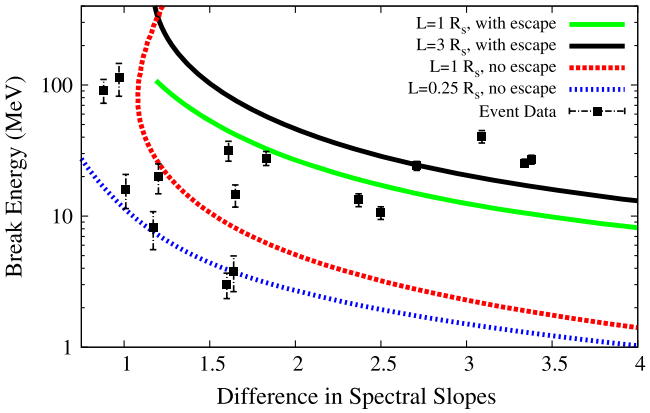

Figure 12. Observed and predicted values of the break energy as a function of the difference of spectral slopes, $|\gamma_2 - \gamma_1|$. Events with higher break energies should have harder spectra and weaker rigidity dependence.

include escape. Escape likely becomes important for larger injection regions associated with amply sized shocks ($>1\ R_s$). Conversely, smaller injection regions ($<1\ R_s$) may be associated with more localized CMEs. Escape from such structures may be difficult due to the rapid expansion of the acceleration region.

Recently, Desai et al. (2015) fitted the ~0.03–500 MeV nuc^{-1} energy spectra with the double power-law Band function and obtained values for the low-energy and high-energy spectral indices and break energies for 11 species (H–Fe) in 46 large gradual SEP events. The vast majority of these 46 events were observed when the S/C were magnetically well connected to the Sun, and therefore presumably to the solar source regions, and none were accompanied by energetic storm particles (ESPs) or the local interplanetary-shock-associated components. These events were specifically selected to study properties of SEP events for which the acceleration processes occur remotely at CME shocks in the solar corona and the inner heliosphere. Seven of the 46 SEP events surveyed by Desai et al. (2015) were associated with GLEs and are among the 16 GLEs studied by Mewaldt et al. (2012). As in the case of the GLEs, the events studied by Desai et al. (2015) show a distribution of spectral indices consistent with our analysis. In particular, the higher-energy spectral slope has an average $\gamma_2 \approx 3.3$ and a typical range of 2–5. Moreover, the analysis here suggests that the observed range of α_b should be between 0 and 2 (see Equation (20)), which is also consistent with the distribution of α_b obtained from power-law fits to the break energy versus the Q/M ratio of 11 species in each of the 46 SEP events by Desai et al. (2015).

4. DISCUSSION AND CONCLUSIONS

Recent MHD simulations of CME expansion show the formation of strong compression regions and shocks at low coronal heights, $<2\ R_\odot$. These compressions and shocks form due to the rapid expansion and acceleration of the CME and then subside higher in the corona where the CME acceleration slows.

We developed a model of particle acceleration at a low coronal shock or compression with a finite size (length L) and a fixed field-flow angle. Results of the model show the pronounced effects of particle diffusion and particle escape, leading to double power-law distributions. The slope of the power law below the spectral break is roughly consistent with steady diffusive shock acceleration. However, above the spectral break, the spectral slope is strongly controlled by the rigidity dependence in the diffusion coefficients.

We performed an initial examination of these results in the context of observations of SEP events. The observations appear roughly consistent with the model. The approach taken here provides a potentially straightforward interpretation of broken power-law distributions from large SEP events and a number of important testable properties. The latter should help to spur on future studies comparing observations, theories, and models of energetic particle acceleration and propagation.

The break energy and the higher-energy power law are both strong functions of the rigidity dependence of the scattering mean free path, which can be determined by the charge-to-mass dependence of the break energy. For example, strong rigidity dependence in the scattering mean free path reduces the break energy and softens the spectrum above the break energy. The spectral index above the break energy is controlled by diffusion away from the injection region and escape, which participates in steepening the spectral slope above the break energy.

Application of the concepts developed here to SEP observations suggest a number of tentative conclusions. First, examination of the spectral slopes below the break energy suggests compression ratios at shocks in the range of $r_c = 2 - 4$. Second, analysis of the charge-to-mass dependence in spectral slopes suggests rigidity dependence in the scattering mean free path, where $\lambda_{\|} \propto R_g^{\chi}$ and the typical range of $\chi = 0.5 - 7$. For $\chi < 1$, diffusion is weakly rigidity dependent, consistent with quasi-perpendicular shocks (Li et al. 2009). In the opposite limit of $\chi > 1$, diffusion is strongly rigidity dependent, consistent with quasi-parallel shocks (Li et al. 2009; Battarbee et al. 2011, 2013; Vainio et al. 2014). The wide range of characteristics suggests competing mechanisms at work in SEP acceleration.

An important feature of the structures that accelerate particles from the low corona is the buildup of the quasi-perpendicular field compression at the front of the CME expansion. The fact that this sheath is draped by magnetic fields containing the plasma that is swept up by the CME suggests that this region should be effective at storing particle populations released prior to the CME injection. Therefore, these sheaths may naturally build up He^3 and heavy ions (e.g., Fe) released by flares. Subsequent acceleration near the shock or compression would thereby enhance such populations that build up within the sheath.

Thus, we find that strong compressions and shocks in the low corona may naturally create broken power-law distributions that arise in large SEP events. Cases in which shocks are very strong naturally yield more efficient particle acceleration and weak rigidity dependence in particle diffusion coefficients.

We thank all those who made C-SWEPA (NASA grant NNX13AI75G), EMMREM (grant NNX07AC14G), Sun-2-Ice (NSF grant AGS1135432), DREAM (NASA grant NNX10AB17A), and DREAM2 (NASA grant NNX14AG13A) projects possible. Data for all figures can be obtained by contacting the lead author, N. Schwadron. The contributions of T.T., C.D., R.L., J.A.L., Z.M., and P.R. were supported by the NSF Frontiers in Earth System Dynamics program and the Center for Integrated Space Weather Modeling, and by NASA's SBIR, HTP, LWS, and SR&T

programs. Computational resources were provided by the NSF supported Texas Advanced Computing Center (TACC) in Austin and the NASA Advanced Supercomputing Division (NAS) at Ames Research Center.

APPENDIX A
MHD SIMULATION OF A FAST CME

The CME simulation employed for our analysis, also used in Lionello et al. (2013), will be described in detail in a forthcoming publication (T. Török et al. 2015, in preparation). Here we restrict ourselves to a brief summary of its main properties.

The simulation is performed using the Magnetohydrodynamic Algorithm outside a Sphere (MAS) code (e.g., Mikić & Linker 1994; Linker et al. 1999; Lionello et al. 1999; Mikić et al. 1999). The code uses spherical coordinates and advances the standard viscous and resistive MHD equations. It incorporates radiative losses, thermal conduction parallel to the magnetic field, and an empirical coronal heating function. The latter properties are essential for realistic modeling of the plasma densities and temperatures in the corona and provide the possibility of producing synthetic EUV and soft X-ray images that can directly be compared to the observations (see Lionello et al. 2009).

The simulation domain covers the solar corona between 1 and 20 R_s, where R_s is the solar radius. The grid is nonuniform in $r \times \theta \times \phi$, resolved by $251 \times 301 \times 261$ points, with $r \approx 0.3$ Mm at the lower radial boundary and $r \approx 153$ Mm at 20 R_s. The latitudinal (longitudinal) mesh varies between $\theta \approx \phi \approx 1.4$ Mm in the active region (AR) center and $\theta \approx 46$ Mm ($\phi \approx 42$ Mm) far from the AR. The boundary conditions are discussed by Linker & Mikić (1997) and Linker et al. (1999).

The Alfvén travel time at the base of the corona ($\tau_A = R_s/V_A$) for $|B| = 2.207$ G and $n_0 = 10^8\,\mathrm{cm}^{-3}$, which are typical reference values, is 24 minutes (Alfvén speed $V_A = 481\,\mathrm{km\,s}^{-1}$). A uniform resistivity is chosen such that the Lundquist number τ_R/τ_A is 1.0×10^7, where τ_R is the resistive diffusion time. A uniform viscosity ν is used, corresponding to a viscous diffusion time τ_ν such that $\tau_\nu/\tau_A = 500$. This value is chosen to dissipate unresolved scales without substantially affecting the global solution. During our model eruption, when strong reconnection occurs below the erupting CME, we locally increase the resistivity and viscosity to values required to keep the calculation numerically stable.

We consider an idealized coronal magnetic configuration, consisting of a global dipole with a field strength of 2 G at the poles and a quadrupolar active region (AR) located at ≈25° north of the equator. We choose a quadrupolar AR since CMEs from such regions tend to produce faster CMEs than bipolar source regions (e.g., Török & Kliem 2007; Wang & Zhang 2008). After an MHD solution including a solar wind is obtained by relaxing the system for 150 τ_A to a steady state (see Lionello et al. 2009), we insert a modified version of the flux rope model by Titov & Démoulin (1999, hereafter TDM) above the central polarity inversion line (PIL) of the AR. Including the flux rope, the model AR has a total unsigned flux of $\approx 7.5 \times 10^{22}$ Mx and a maximum radial-field strength of ≈1070 G at the photospheric level.

In contrast to previous CME simulations that employed the Titov–Démoulin model (e.g., Manchester et al. 2008; Lugaz et al. 2011), we do not use an unstable flux rope to trigger the CME. Rather, we choose the parameters of the inserted TDM rope such that it is stabilized by the AR's ambient magnetic field. After the insertion, we relax the system for another $32\tau_A$, which allows the wave-like perturbation caused by the insertion to travel out of the numerical domain. After a fast and strongly dynamic initial adjustment to the surrounding magnetic field, the flux rope evolves toward a numerical equilibrium. This novel technique of flux rope insertion is detailed by Titov et al. (2014). After the relaxation, the free magnetic energy of the AR is about 1.0×10^{33} erg, which is sufficient to power a strong eruption.

The CME is initiated by triggering the eruption of the TDM flux rope. This is done by imposing slow, localized photospheric converging flows toward the main PIL (e.g., Bisi et al. 2010) for about 45 minutes [$t = (182 - 183.8)\,\tau_A$]. These motions cancel flux at the PIL and quasi-statically expand the magnetic field overlying the flux rope. As a consequence of the progressively reduced magnetic tension, the rope rises slowly, until it reaches a critical height at which it becomes unstable and erupts (e.g., Kliem & Török 2006; Aulanier et al. 2010; Török et al. 2011). Aided by the strong (flare) reconnection jets that occur below the erupting rope, the resulting CME rapidly accelerates to a velocity of $\approx 3000\,\mathrm{km\,s}^{-1}$ low in the corona ($r \lesssim 2\,R_s$), after which it slows down and finally travels with an almost constant speed of $\approx 1000\,\mathrm{km\,s}^{-1}$ at heights $r \gtrsim 3R_s$. We coupled this simulation to the heliospheric version of MAS and propagated the eruption up to 1 AU (Lionello et al. 2013). We found that the CME arrives at 1 AU with a speed of $\approx 600\,\mathrm{km\,s}^{-1}$, still moving significantly faster than the surrounding slow solar wind.

The eruption feature most relevant for our investigation is the large-scale compression region that forms in front of the CME and at its flanks. Figure 1 shows a snapshot of the erupting flux rope together with the local plasma velocity and $\nabla \cdot \boldsymbol{v}$ (which shows regions with the strongest compression). While not pertinent to the present investigation, the figure also reveals the strong compression associated with the flare reconnection jets in the wake of the CME.

APPENDIX B
EFFECTIVE PARALLEL AND PERPENDICULAR SCATTERING MEAN FREE PATHS

The diffusion tensor is given by

$$\mathsf{K} = \kappa_\parallel \hat{e}_b \hat{e}_b + \kappa_\perp \left(\mathsf{I} - \hat{e}_b \hat{e}_b\right), \tag{22}$$

where $\kappa_\parallel$ and $\kappa_\perp$ are the diffusion coefficients parallel and perpendicular to the magnetic field, respectively.

In this study, we consider a range of different ratios of perpendicular to parallel diffusion of $\kappa_\perp/\kappa_{s,\parallel}$, where $\kappa_{s,\parallel} = v\lambda_\parallel/3$ is the parallel diffusion coefficient associated with scattering through wave–particle interaction. The recommended range of some previous studies is (0.01–0.05) (e.g., Giacalone & Jokipii 1999). However, there is considerable uncertainty about the value or range of the $\kappa_\perp/\kappa_\parallel$ and its dependence on particle energy. For example, in one recent study, Zank et al. (2006) finds a value as small as $\kappa_\perp/\kappa_\parallel \sim 0.001$.

Supergranulation reconfiguration timescales are typically $\tau_r \sim 1$ day. This implies a random walk diffusion coefficient associated with reconfiguration of the magnetic field given by

$$D_r\left(R_s\right) = l^2/(u\tau_r), \tag{23}$$

where $l \sim 20{,}000$ km is the size-scale of a supergranule and $u \sim 400\,\mathrm{km\,s^{-1}}$ is the solar wind speed. Jokipii & Parker (1969) argued that the random walk of field lines above the photosphere should yield a diffusion coefficient that scales with the square of the radius, $D_r(r) = D_r(R_s)(r/R_s)^2$. The perpendicular scattering mean free path is then $\lambda_\perp \sim 3D_r(r)$, and the associated perpendicular diffusion coefficient is $\kappa_\perp \sim \lambda_\perp v/3$. At an energy of 1 MeV, this would yield a ratio of $\kappa_\perp/\kappa_\parallel \sim 2.5 \times 10^{-5}$, many orders of magnitude smaller than the values cited above (0.001–0.05). As a result, we consider a range of different levels for $\kappa_\perp/\kappa_\parallel$ ranging from 10^{-5} to 0.01.

APPENDIX C
PARTICLE INJECTION

In this and the following appendices, we consider the presence and effects of a shock on the acceleration of solar energetic particles. For the purposes of these calculations, there is no stringent requirement that the structure actually be a shock. A sharp compression would also lead to the strong gradients needed for rapid particle acceleration.

We consider a magnetic field line (or flux bundle) that makes an angle θ_1 to the shock normal upstream and an angle θ_2 downstream of the shock. We take u_1 to be the plasma velocity component normal to the shock. The connection between the shock and the magnetic flux bundle moves at a speed $u_1 \tan(\theta_1)$ along the shock and at a speed $u_1/\cos(\theta_1)$ along the magnetic flux bundle. Hence, the parallel injection speed is the minimum speed for particles needed to keep up with the shock connection along the magnetic flux bundle,

$$v_{||\mathrm{inj}} = \frac{u_1}{\cos\left(\theta_1\right)}. \tag{24}$$

Because the shock may have values of θ_1 close to 90°, we must also take into account the motion of particles across magnetic field lines. This significantly reduces the injection speed because particles may take a more direct path across magnetic field lines to cross the shock. To work out the injection speed in this case, including the effects of perpendicular diffusion, it is necessary to develop an expression for the diffusive anisotropy, which characterizes the particle distribution's departure from isotropy. The anisotropy is expressed as $\boldsymbol{\delta} = 3\boldsymbol{S}/(vf_0)$, where the particle streaming is $\boldsymbol{S}$, the isotropic part of the distribution is f_0, and the particle speed is v. An expression for the anisotropy can be solved for as an analytical solution to the Parker transport equation. Here, we express the magnitude of the anisotropy (Giacalone 2001):

$$\delta = \frac{3u_1}{v} \left[1 + \frac{(\kappa_A/\kappa_{||})^2 \sin^2\theta_1 + \left(1 - \kappa_\perp/\kappa_{||}\right)^2 \sin^2\theta_1 \cos^2\theta_1}{\left((\kappa_\perp/\kappa_{||})\sin^2\theta_1 + \cos^2\theta_1\right)^2}\right]^{1/2}, \tag{25}$$

where $\kappa_\parallel$ and $\kappa_\perp$ are the diffusion coefficients parallel and perpendicular to the mean magnetic field, respectively. The antisymmetric component of the diffusion tensor is $\kappa_A = vr_g/3$ and contains the effect of drifts. A general condition on the validity of the theory of diffusive shock acceleration is that the magnitude of the anisotropy must be small. If this condition breaks down, particles do not rapidly scatter across the shock, and the shock acceleration process slows. The injection speed can be solved for by requiring that the anisotropy magnitude is less than a quantity of order unity. Here, we express this condition as $\delta < 3$, where the factor of 3 is chosen so that the resulting injection speed,

$$v_{\mathrm{inj}} = u_1 \left[1 + \frac{(\kappa_A/\kappa_{||})^2 \sin^2\theta_1 + \left(1 - \kappa_\perp/\kappa_{||}\right)^2 \sin^2\theta_1 \cos^2\theta_1}{\left((\kappa_\perp/\kappa_{||})\sin^2\theta_1 + \cos^2\theta_1\right)^2}\right]^{1/2}, \tag{26}$$

yields the parallel injection speed (24) in the limit that $\kappa_\perp \to 0$ and $\kappa_A \to 0$.

APPENDIX D
DIFFUSIVE ACCELERATION ANALYTICAL SOLUTION

Our approach to understanding the influence of shock structure on the evolution of distribution functions at the shock follows closely from the solution applied by Schwadron et al. (2008) for the termination shock.

Here, we first use Fourier analysis to solve for the distribution function at the shock given injection at a single point along the shock and a finite angle (θ) between the shock normal and the magnetic field. We find that this solution contains many of the essential properties needed to understand the combined effects of particle motion, diffusion, and acceleration along the shock. The main difference between this approach and that used by Schwadron et al. (2008) is the form of the mean free path, which we now take to depend on particle rigidity. The previous treatment by Schwadron et al. (2008) assumed a constant scattering mean free path.

In the following, we use expressions for the diffusion coefficients along x and z where

$$\kappa_{xx} = \kappa_\parallel \cos^2\theta + \kappa_\perp \sin^2\theta, \tag{27}$$

$$\kappa_{xz} = (\kappa_\parallel - \kappa_\perp)\sin\theta\cos\theta, \tag{28}$$

$$\kappa_{zz} = \kappa_\parallel \sin^2\theta + \kappa_\perp \cos^2\theta. \tag{29}$$

As mentioned previously, we have not included an off-diagonal term, κ_A, due to drift that is sometimes included in the diffusion tensor. Instead of including the drift term in the diffusion tensor, an explicit drift term, $\nabla \cdot [cvp\boldsymbol{B}/(3qB^2) \times \nabla f]$, may be included on the left-hand side of the Parker equation. Such a treatment is considered in Appendix D.2. Generally, drift leads to motion out of the coplanarity plane. However, the effect tends to be small, except for shocks or compressions with obiquity angles very close to 90°.

D.1. Solution in the Coplanarity Plane

Consider the steady state injection of particles at a shock at position $z = 0$ and $x = 0$ with momentum p_{inj}. The differential equation in this case is as follows:

$$\boldsymbol{u}\cdot\nabla f - \nabla\cdot(\mathsf{K}\cdot\nabla f) - \frac{\nabla\cdot\boldsymbol{u}}{3}p\frac{\partial f}{\partial p} = Q_0\delta(x)\delta(z)\delta(p - p_{\mathrm{inj}}), \tag{30}$$

where

$$\mathsf{K} = \kappa_\parallel \hat{e}_b\hat{e}_b + \kappa_\perp\left(\mathsf{I} - \hat{e}_b\hat{e}_b\right). \tag{31}$$

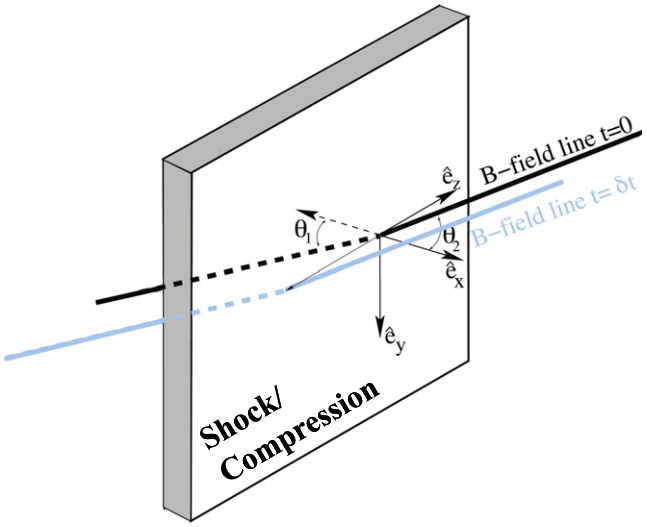

Figure 13. Schematic diagram of magnetic flux bundle piercing a shock or compression region at two times. The black flux bundle is shown at an initial time ($t = 0$), and the blue line represents the flux bundle at some small time ($t = \delta t$) later.

As shown in Figure 13, we take (x, z) as the coplanarity plane and no dependence on y, so that cross-field drifts do not appear.

The source term is a slight modification of the standard treatment for diffusive shock acceleration theory. The shock or compression is within a plane $(y - z)$ centered at $x = 0$. Magnetic field lines lie within the $x - z$ plane (coplanarity). The constant Q_0 scales the injection of particles,

$$Q_0 = u_1 \epsilon f_{\rm inj} L p_{\rm inj}, \tag{32}$$

where ϵ is the injection efficiency, $f_{\rm inj}$ is the distribution function at the injection energy, and L is size-scale of the shock.

We expand the differential equation as follows:

$$\begin{aligned} u_x \frac{\partial f}{\partial x} + u_z \frac{\partial f}{\partial z} &- \nabla \cdot \left(\kappa_\perp \mathrm{I} \cdot \nabla f\right) \\ &- \nabla \cdot \left[\hat{e}_b (\kappa_\parallel - \kappa_\perp) \hat{e}_b \cdot \nabla f\right] \\ &+ \frac{u_{x1} - u_{x2}}{3} \delta(x) p \frac{\partial f}{\partial p} \\ &= Q_0 \delta(x) \delta(z) \delta(p - p_{\rm inj}). \end{aligned} \tag{33}$$

We then Fourier transform the differential equation, with the following convention for the Fourier integral:

$$f(z, x, p) = \frac{1}{2\pi} \int_{-\infty}^{\infty} dk \, \exp(ikz) \, \tilde{f}(k, x, p). \tag{34}$$

The Fourier-transformed differential equation then becomes

$$\begin{aligned} u_x \frac{\partial \tilde{f}}{\partial x} &+ iku_z \tilde{f} + k^2 \kappa_{zz} \tilde{f} \\ &- \frac{\partial}{\partial x}\left(\kappa_{xx} \frac{\partial \tilde{f}}{\partial x}\right) - \frac{\partial}{\partial x}\left[\kappa_{xz} ik \tilde{f}\right] \\ &- ik\kappa_{xz} \frac{\partial \tilde{f}}{\partial x} + \delta(x) \frac{u_{1x} - u_{2x}}{3} \frac{\partial \tilde{f}}{\partial \ln p} \\ &= Q_0 \delta(x) \delta(p - p_{\rm inj}). \end{aligned} \tag{35}$$

For $x \neq 0$, we take $\tilde{f} \propto \exp(\alpha x)$, which leads to the following quadratic equation that is solved upstream and downstream

$$-\alpha^2 \kappa_{xx} + \alpha\left(u_x - 2ik\kappa_{xz}\right) + iku_z + k^2 \kappa_{zz} = 0. \tag{36}$$

The upstream ($j = 1$) and downstream ($j = 2$) solutions are as follows:

$$\begin{aligned} \alpha_j = \frac{u_{xj}}{2\kappa_{xxj}} &- ik\frac{\kappa_{xzj}}{\kappa_{xxj}} + \frac{(-1)^{j+1}}{\kappa_{xxj}} \\ &\times \sqrt{u_{xj}^2/4 + \kappa_{\parallel j}\kappa_{\perp j} k^2 + ik(\kappa_{xxj} u_{zj} - \kappa_{xzj} u_{xj})}. \end{aligned} \tag{37}$$

The signs, $(-1)^{j+1}$, are chosen for convergence: for $k = 0$, they must give the result for a stationary shock.

Given the solution for α_j, we now integrate (35) from the upstream to the downstream side of the shock. This integral extends over a narrow region centered on the shock jump, and therefore pulls out only quantities that change almost discontinuously across the shock. As a result, we recover the following equation:

$$\begin{aligned} -(\kappa_{xx2}\alpha_2 - \kappa_{xx1}\alpha_1)\tilde{f} &- (\kappa_{xz2} - \kappa_{xz1}) ik\tilde{f} \\ &+ \frac{\Delta u}{3} \frac{\partial \tilde{f}}{\partial \ln p} = Q_0 \delta(p - p_{\rm inj}). \end{aligned} \tag{38}$$

Note that

$$\begin{aligned} (\kappa_{xx2}\alpha_2 - \kappa_{xx1}\alpha_1) + (\kappa_{xz2} - \kappa_{xz1}) ik &= -\frac{\Delta u}{2} \\ &- \sum_{j=1}^{2} \sqrt{\frac{u_{xj}^2}{4} + \kappa_{\parallel j}\kappa_{\perp j} k^2 + ik(\kappa_{xxj} u_{zj} - \kappa_{xzj} u_{xj})}. \end{aligned} \tag{39}$$

With the solutions upstream and downstream from the shock, we can now express the solution for $\tilde{f}(k, p)$, and, in turn, the distribution function at the shock

$$\begin{aligned} f_s(z, p) = \frac{3Q_0}{2\pi \Delta u p_{\rm inj}} &\left(\frac{p}{p_{\rm inj}}\right)^{-3/2} \int_{-\infty}^{\infty} dk \\ &\times \exp\left(ikz - \frac{3}{\Delta u} \int_{\ln p_{\rm inj}}^{\ln p} d \ln p' \sum_{j=1}^{2} \right. \\ &\left. \times \sqrt{\frac{u_{xj}^2}{4} + \kappa_{\parallel j}\kappa_{\perp j} k^2 + ik(\kappa_{xxj} u_{zj} - \kappa_{xzj} u_{xj})}\right), \end{aligned} \tag{40}$$

where $\Delta u = u_{1x} - u_{2x}$. Up to this point in the derivation, the steps are identical as those performed in (Schwadron et al. 2008, Appendix B).

The departure in the derivation comes when treating the diffusion mean free paths, which are proportional to a power-law in speed $\lambda \propto v^\chi$. Noting that the square root in (40) equals $u_{xj}/2$ as $k \to 0$, we add and subtract $u_{xj}/2$ from the square root;

the $\ln p$-integral of $u_{xj}/2$ is trivial, and we obtain

$$f_s(z,p) = \frac{3Q_0}{2\pi\Delta u p_{\rm inj}}\left(\frac{p}{p_{\rm inj}}\right)^{-\gamma}\int_{-\infty}^{\infty} dk\ \exp(ikz) \times \exp\left(-\frac{3}{\Delta u}\int_{\ln p_{\rm inj}}^{\ln p} d\ln p' \sum_{j=1}^{2} \times \left[\sqrt{\frac{u_{xj}^2}{4} + \kappa_{\parallel j}\kappa_{\perp j}k^2 + ik(\kappa_{xxj}u_{zj} - \kappa_{xzj}u_{xj})} - \frac{u_{xj}}{2}\right]\right), \quad (41)$$

where $\gamma = 3r_c/(r_c - 1)$ is the standard power-law index of diffusive shock acceleration. Assuming that the protons are non-relativistic so that $p \approx mv$, and noting that the square root is a function of $k(v')^{\chi+1}$, we rewrite (41) as

$$f_s(z,p) = \frac{3Q_0}{2\pi\Delta u p_{\rm inj}}\left(\frac{v}{v_{\rm inj}}\right)^{-\gamma}\frac{1}{v^{\chi+1}}\int_{-\infty}^{\infty} d\eta \times \exp\left[i\eta\left(z/v^{\chi+1}\right) - \frac{3}{(\chi+1)\Delta u} \times \int_{-\infty}^{\ln(\eta)} d\ln\xi \sum_{j=1}^{2} \times \left\{\sqrt{\frac{u_{xj}^2}{4} + \frac{\tau_{\parallel j}\tau_{\perp j}}{9}\xi^2 + i\xi\left(\frac{\kappa_{xxj}}{v^{\chi+1}}u_{zj} - \frac{\kappa_{xzj}}{v^{\chi+1}}u_{xj}\right)} - \frac{u_{xj}}{2}\right\}\right], \quad (42)$$

where $\xi = k(v')^{\chi+1}$, $\eta = kv^{\chi+1}$, $\kappa_\parallel = \tau_\parallel v^{\chi+1}/3$, $\kappa_\perp = \tau_\perp v^{\chi+1}/3$, and the lower limit of the ξ-integration has been replaced by minus infinity since the integrand is convergent as $kv_{\rm inj}^{\chi+1} \to 0$.

The η-integral is only a function of $z/v^{\chi+1}$. If $v^{\chi+1}/z > \eta_0$, where η_0 is the scale for the decay of the integrand of the η-integration, then the factor $\exp[i\eta(z/v^{\chi+1})] \approx 1$ and (42) yield the high-energy power-law spectrum $f_s \propto v^{-\gamma-1-\chi}$. For small and intermediate values of $v^{\chi+1}/z$ ($v^{\chi+1}/z \ll \eta_0$ and $v^{\chi+1}/z \sim \eta_0$), we may expand the integrand of the ξ-integration in powers of ξ and retain terms up to order ξ^2. The ξ-integral may then be evaluated to yield

$$f_s(z,p) = \frac{3Q_0}{2\pi\Delta u p_{\rm inj}}\left(\frac{v}{v_{\rm inj}}\right)^{-\gamma}\frac{1}{v^{\chi+1}} \times \int_{-\infty}^{\infty} d\eta \exp\left[i\eta\frac{z}{v^{\chi+1}} - \frac{3}{(\chi+1)\Delta u}\left(i\eta a + \eta^2 b/4\right)\right], \quad (43)$$

where

$$a = \sum_{j=1}^{2}\left[\frac{\kappa_{xxj}u_{zj}}{v^{chi+1}u_{xj}} - \frac{\kappa_{xzj}}{v^{\chi+1}}\right] \quad (44)$$

$$b = \sum_{j=1}^{2}\left\{2\frac{\tau_{\parallel j}\tau_{\perp j}}{9u_{xj}} + \frac{2}{u_{xj}}\left[\frac{\kappa_{xxj}u_{zj}}{v^{\chi+1}u_{xj}} - \frac{\kappa_{xzj}}{v^{\chi+1}}\right]^2\right\}. \quad (45)$$

The remaining integration in (43) can be evaluated by "completing the square" in the argument of the exponential function. We then obtain the following:

$$f_s(z,p) \approx \frac{3Q_0}{2\pi\Delta u p_{\rm inj}}\left(\frac{v}{v_{\rm inj}}\right)^{-\gamma}\frac{1}{v^{\chi+1}}\sqrt{\frac{8\pi\Delta u}{3b}} \times \exp\left\{-\left[\frac{z}{v^{\chi+1}} - \frac{3a}{(\chi+1)\Delta u}\right]^2 \times \left(\frac{(\chi+1)\Delta u}{3b}\right)\right\}. \quad (46)$$

The only difference between (46), evaluated for small $z/v^{\chi+1}$, and (42) with $(z/v^{\chi+1}) = 0$, which yields the correct asymptotic energy spectrum, is the expansion of the square root in powers of ξ up to order ξ^2.

Equation (46) demonstrates the physical nature of diffusive acceleration on flux bundles with a moving point of shock intersection. Since it takes time for ions to be accelerated to progressively higher energies, the peak of the distribution of ions must move from the point of injection to progressively more distant regions on the flank of the shock. Therefore,

$$z_d = \frac{3av^{\chi+1}}{(\chi+1)\Delta u} \quad (47)$$

is the distance moved along the shock from the injection point by the majority of ions in the process of being accelerated to a given energy. The average ion speed along the shock is

$$V_{sz} = \frac{dz_d}{d\tau_p}, \quad (48)$$

where τ_p is the characteristic time it takes to accelerate ions to momentum p, and $d\tau_p$ is the infinitesimal time required to accelerate ions from momentum p to $p + dp$:

$$d\tau_p = \frac{3\delta x}{\Delta u}\frac{dp}{p}, \quad (49)$$

and the characteristic width of the acceleration region is

$$\delta x = \frac{\kappa_{xx1}}{u_{x1}} + \frac{\kappa_{xx2}}{u_{x2}}. \quad (50)$$

Therefore, using (48) and (49), we solve for the average particle motion along the shock

$$V_{sz} = \frac{\Delta u}{3\delta x}\frac{dz_d}{d\ln p} = \frac{v^{\chi+1}a}{\delta x}. \quad (51)$$

The solution for f_s is written in the form of a diffusive solution,

$$f_s(z,p) \approx \frac{3Q_0}{2\pi\Delta u p_{\rm inj}}\left(\frac{v}{v_{\rm inj}}\right)^{-\gamma}\sqrt{\frac{\pi}{D_z}}\exp\left\{-\frac{(z-z_d)^2}{4D_z}\right\}, \quad (52)$$

where the characteristic width of the Gaussian distribution in Equation (46) is

$$D_z = \frac{3bv^{2(\chi+1)}}{4(\chi+1)\Delta u}. \quad (53)$$

The average diffusion rate along the shock is

$$K_{szz} = \frac{dD_z}{d\tau_p} = \frac{bv^{2(\chi+1)}}{2\delta x}. \quad (54)$$

D.2. Solution out of the Coplanarity Plane

The differential equation for particle transport and acceleration out of the coplanarity plane includes the curvature and gradient drifts from the magnetic field:

$$\boldsymbol{u}\cdot\nabla f - \nabla\cdot(\mathsf{K}\cdot\nabla f) + \nabla\cdot\left(\frac{cvp}{3q}\frac{\boldsymbol{B}}{B^2}\times\nabla f\right) - \frac{\nabla\cdot\boldsymbol{u}}{3}p\frac{\partial f}{\partial p} = Q_0\delta(x)\delta(y)\delta(p-p_{\rm inj}). \quad (55)$$

We take (x, y) as the coordinates out of the coplanarity plane and no dependence on z so that now cross-field drifts appear. We expand the differential equation as follows:

$$u_x\frac{\partial f}{\partial x} + u_y\frac{\partial f}{\partial y} - \nabla\cdot\left(\kappa_\perp \mathsf{I}\cdot\nabla f\right) - \nabla\cdot\left[\hat{e}_b(\kappa_\parallel-\kappa_\perp)\hat{e}_b\cdot\nabla f\right] - \frac{cvp}{3q}\left(\frac{B_{2z}}{B_2^2}-\frac{B_{1z}}{B_1^2}\right)\delta(x)\frac{\partial f}{\partial y} + \frac{u_{x1}-u_{x2}}{3}\delta(x)p\frac{\partial f}{\partial p} = Q_0\delta(x)\delta(y)\delta(p-p_{\rm inj}). \quad (56)$$

We then Fourier transform the differential equation, with the Fourier transform defined as

$$f(y,x,p) = \frac{1}{2\pi}\int_{-\infty}^{\infty} dk\ \exp(iky)\,\tilde{f}(k,x,p). \quad (57)$$

The Fourier-transformed differential equation then becomes

$$u_x\frac{\partial\tilde{f}}{\partial x} + iku_y\tilde{f} + k^2\kappa_\perp\tilde{f} - \frac{\partial}{\partial x}\left(\kappa_{xx}\frac{\partial\tilde{f}}{\partial x}\right) - ik\delta(x)\frac{cvp}{3q}\left(\frac{B_{2z}}{B_2^2}-\frac{B_{1z}}{B_1^2}\right)\tilde{f} + \delta(x)\frac{u_{1x}-u_{2x}}{3}\frac{\partial\tilde{f}}{\partial\ln p} = Q_0\delta(x)\delta(p-p_{\rm inj}). \quad (58)$$

For $x\neq 0$, we take $\tilde{f}\propto\exp(\alpha x)$, which leads to the following quadratic equation that is solved upstream and downstream:

$$-\alpha^2\kappa_{xx} + \alpha u_x + iku_y + k^2\kappa_\perp = 0. \quad (59)$$

The upstream ($j=1$) and downstream ($j=2$) solutions are as follows:

$$\alpha_j = \frac{u_{xj}}{2\kappa_{xxj}} + \frac{(-1)^{j+1}}{\kappa_{xxj}}\sqrt{u_{xj}^2/4 + \kappa_{xxj}\left(iku_{yj}+\kappa_{\perp j}k^2\right)}. \quad (60)$$

The signs, $(-1)^{j+1}$, are chosen for convergence: for $k=0$, they must give the result for a stationary shock.

With the solutions upstream and downstream from the shock, we integrate from the upstream to downstream side of the shock, drawing out the terms that are almost discontinuous. As in the previous subsection, we then solve a first-order differential equation in terms of the momentum to derive the solution for the distribution function at the shock

$$f_s(y,p) = \frac{3Q_0}{2\pi\Delta up_{\rm inj}}\left(\frac{p}{p_{\rm inj}}\right)^{-3/2}\int_{-\infty}^{\infty}dk \times\exp\left(iky + ik\frac{c}{q\Delta u}\left[\frac{B_{2z}}{B_2^2}-\frac{B_{1z}}{B_1^2}\right]\int_{\ln p_{\rm inj}}^{\ln p} d\ln p'\ p'v'\right) \times\exp\left(-\frac{3}{\Delta u}\int_{\ln p_{\rm inj}}^{\ln p}\sum_{j=1}^{2}d\ln p' \times\sqrt{u_{xj}^2/4+\kappa_{xxj}\kappa_{\perp j}k^2+ik\kappa_{xxj}u_{yj}}\right), \quad (61)$$

where $\Delta u = u_{1x}-u_{2x}$. As before, we introduce variables $\eta = kv^{\chi+1}$, $\xi = k(v')^{\chi+1}$, assume non-relativistic energies ($p=mv$), and rewrite the integral as follows:

$$f_s(y,p) = \frac{3Q_0}{2\pi\Delta up_{\rm inj}}\left(\frac{v}{v_{\rm inj}}\right)^{-\gamma}\frac{1}{v^{\chi+1}}\int_{-\infty}^{\infty}d\eta \times\exp\left(i\eta\frac{y}{v^{\chi+1}} + i\eta\frac{mc}{\Delta uq}\left[\frac{B_{2z}}{B_2^2}-\frac{B_{1z}}{B_1^2}\right]\frac{v^2-v_{\rm inj}^2}{2v^{\chi+1}} - \frac{3}{(\chi+1)\Delta u}\times\int_0^{\ln\eta}\sum_{j=1}^{2}d\ln\xi \times\left\{\sqrt{u_{xj}^2/4+\frac{\kappa_{xxj}\kappa_{\perp j}}{(v')^{2(\chi+1)}}\xi^2+i\xi\frac{\kappa_{xxj}}{(v')^{\chi+1}}u_{yj}} - \frac{u_{xj}}{2}\right\}\right). \quad (62)$$

The η-integral is only a function of $y/v^{\chi+1}$. If $y/v^{\chi+1}>\eta_0$, where η_0 is the scale for the decay of the integrand of the η-integration, then the factor $\exp[i\eta(y/v^{\chi+1})]\approx 1$ and (42) yield the high-energy power-law spectrum $f_s\propto v^{-\gamma-\chi-1}$. For small and intermediate values of $y/v^{\chi+1}$ ($y/v^{\chi+1}\ll\eta_0$ and $y/v^{\chi+1}\sim\eta_0$), we expand the integrand of the ξ-integration in powers of ξ and retain terms up to order ξ^2. The ξ-integral may then be evaluated to yield

$$f_s(y,p) = \frac{3Q_0}{2\pi\Delta up_{\rm inj}}\left(\frac{v}{v_{\rm inj}}\right)^{-\gamma}\frac{1}{v^{\chi+1}} \times\int_{-\infty}^{\infty}d\eta\ \exp\left\{i\eta\frac{y}{v^{\chi+1}} + i\eta\frac{mc}{\Delta uq}\left[\frac{B_{2z}}{B_2^2}-\frac{B_{1z}}{B_1^2}\right] \times\frac{v^2-v_{\rm inj}^2}{2v^{\chi+1}} - \frac{3}{(\chi+1)\Delta u}\left(i\eta a' + \eta^2 b'/4\right)\right\}, \quad (63)$$

where

$$a' = \sum_{j=1}^{2}\frac{\kappa_{xxj}u_{yj}}{v^{\chi+1}u_{xj}} \quad (64)$$

$$b' = 2\sum_{j=1}^{2}\left\{\frac{\kappa_{xxj}\kappa_{\perp j}}{u_{xj}v^{2(\chi+1)}} + \frac{1}{u_{xj}}\left(\frac{\kappa_{xxj}u_{yj}}{v^{\chi+1}u_{xj}}\right)^2\right\}. \quad (65)$$

The remaining integration in (63) can be evaluated by completing the square in the argument of the exponential

function. We then obtain the following:

$$f_s(y,p) \approx \frac{3Q_0}{2\pi\Delta u p_{inj}}\left(\frac{v}{v_{inj}}\right)^{-\gamma}\frac{1}{v^{\chi+1}}\sqrt{\frac{4\pi(\chi+1)\Delta u}{3b'}} \exp\left\{-\left[\frac{y}{v^{\chi+1}}+\frac{mc}{\Delta u q}\left[\frac{B_{2z}}{B_2^2}-\frac{B_{1z}}{B_1^2}\right]\times\frac{v^2-v_{inj}^2}{2v^{\chi+1}}-\frac{3a'}{(\chi+1)\Delta u}\right]^2\times\left(\frac{(\chi+1)\Delta u}{3b'}\right)\right\}. \quad (66)$$

In this case, the peak of the distribution of ions moves from the point of injection to progressively more distant regions out of the coplanarity plane where injection occurs. Therefore, the average distance moved in the y-direction along the shock for acceleration to a given energy is

$$y_d = -\frac{mc}{\Delta u q}\left[\frac{B_{2z}}{B_2^2}-\frac{B_{1z}}{B_1^2}\right]\frac{v^2-v_{inj}^2}{2}+\frac{3a'v^{\chi+1}}{(\chi+1)\Delta u}. \quad (67)$$

The average ion speed in the y-direction is

$$V_{sy} = \frac{dy_d}{d\tau_p} = \frac{p\Delta u}{3\delta x}\frac{dy_d}{dp} = -\frac{cvp}{3q\delta x}\left(\frac{B_{2z}}{B_2^2}-\frac{B_{1z}}{B_1^2}\right)+\frac{a'v^{\chi+1}}{\delta x}. \quad (68)$$

Jokipii (1982) obtained this result without perpendicular diffusion or transverse plasma velocity. The Jokipii (1982) solution is a delta function in the y-coordinate, shifted by the distance a particle drifts along the shock face.

The solution for f_s is written in the form of a diffusive solution,

$$f_s(z,p) \approx \frac{3Q_0}{2\pi\Delta u p_{inj}}\left(\frac{v}{v_{inj}}\right)^{-\gamma}\times\sqrt{\frac{\pi}{D_y}}\exp\left\{-\frac{(y-y_d)^2}{4D_y}\right\}. \quad (69)$$

The average diffusion rate along the shock in the y-direction, K_{syy}, is the characteristic width of the Gaussian distribution in (69),

$$D_y = \frac{3b'v^{2\chi+2}}{4(\chi+1)\Delta u}. \quad (70)$$

The diffusion rate along the shock in the y-direction is then

$$K_{syy} = \frac{dD_y}{d\tau_p} = \frac{b'v^{2\chi+2}}{2\delta x}. \quad (71)$$

We note that the results here for V_{sy} and K_{syy} are in agreement with expressions for the velocities along Schwadron et al. (2008), with the only difference being the dependence on higher powers of v due to the modified form of the diffusion coefficient.

D.3. Generalized 3D Motion and Diffusion Along the Shock

The expressions for the velocities along the shock, (51) and (68), yield the components of the velocity along the shock in the z- and y-directions, respectively. We combine these expressions into a generalized 3D expression for the average motion along the shock:

$$\boldsymbol{V}_s = \left[\frac{\lambda_1\boldsymbol{u}_1+\lambda_2\boldsymbol{u}_2}{\delta x}-\hat{e}_x\cdot\frac{\mathsf{K}_2+\mathsf{K}_1}{\delta x}+\frac{cvp}{3q\delta x}\hat{e}_x\times\left(\frac{\boldsymbol{B}_2}{B_2^2}-\frac{\boldsymbol{B}_1}{B_1^2}\right)\right]\cdot\left(\mathsf{I}-\hat{e}_x\hat{e}_x\right), \quad (72)$$

where $\lambda_i = \kappa_{xxi}/u_{xi}$. An identical expression was derived by Schwadron et al. (2008). The fact that these expressions are identical despite the differences in the forms of the diffusion coefficient reveals the broader generality of the expression. Similarly, the expressions for the diffusion coefficients (54) and (71) are combined for a generalized expression for the diffusion along the shock:

$$\mathsf{K}_s = \sum_{j=1}^{2}\left\{\frac{\lambda'_j\kappa_{\perp j}}{\delta x}+\frac{\left[\hat{e}_z\cdot\left(\lambda_j\boldsymbol{u}_j-\mathsf{K}_j\cdot\hat{e}_x\right)\right]^2}{u_{xj}\delta x}\right\}\hat{e}_z\hat{e}_z + \sum_{j=1}^{2}\left\{\frac{\lambda_j\kappa_{\perp j}}{\delta x}+\frac{\left[\hat{e}_y\cdot\left(\lambda_j\boldsymbol{u}_j-\mathsf{K}_j\cdot\hat{e}_x\right)\right]^2}{u_{xj}\delta x}\right\}\hat{e}_y\hat{e}_y, \quad (73)$$

where $\lambda'_1 = \kappa_{1\parallel}/u_{1x}$ and $\lambda'_2 = \kappa_{2\parallel}/u_{2x}$.

D.4. Analytical Solution for Fixed Shock Angle

The previous analytical solution (69) is used as a Green's function to solve for the continuous injection of particles at all locations along a shock with a constant shock-normal angle. We integrate for injection from $z' = 0$ to L. The distribution function from the ions injected at the point z_{inj} has the following form:

$$f'_s(z,z_{inj},p) \approx \frac{3Q_0}{2\pi\Delta u p_{inj}}\left(\frac{p}{p_{inj}}\right)^{-\gamma}\times\sqrt{\frac{\pi}{D_z}}\exp\left[-\frac{(z-z_{inj}-z_d)^2}{4D_z}\right]. \quad (74)$$

We obtain our solution for the total distribution, $F_s(z,p)$, by integrating over the locus of injection points distributed from $z_{inj} = 0 \rightarrow L$:

$$F_s(z,p) = \frac{1}{L}\int_0^L dz_{inj} f'_s(z,z_{inj},p) = \frac{3Q_0}{2\Delta u p_{inj}L}\left(\frac{p}{p_{inj}}\right)^{-\gamma}\times\left[\mathrm{erf}\left(\frac{L+z_d-z}{2\sqrt{D_z}}\right)-\mathrm{erf}\left(\frac{z_d-z}{2\sqrt{D_z}}\right)\right]. \quad (75)$$

Based on the geometry, we take

$$Q_0 = u_1\epsilon\, f_{inj}Lp_{inj}, \quad (76)$$

where ϵ is the injection efficiency and $f_{\rm inj}$ is the distribution function at the injection energy.

D.5. Inclusion of Loss Processes in the Coplanarity Plane

In this section, we treat particle acceleration at low coronal shocks and include the loss of energetic particles to the acceleration region. In this case, the transport equation we solve is written as follows:

$$\boldsymbol{u}\cdot\nabla f-\nabla\cdot(\mathsf{K}\cdot\nabla f)-\frac{\nabla\cdot\boldsymbol{u}}{3}p\frac{\partial f}{\partial p}=Q_0\delta(x)\delta(z)\delta(p-p_{\rm inj})-\frac{f}{\tau},\quad(77)$$

where

$$\frac{1}{\tau}=\frac{V_{sz}}{L}.\quad(78)$$

This loss term accounts for the fact that particles are convected across and out of the acceleration region (of length L) on the timescale $1/\tau$. Note in this case that we have considered V_{sz} (Equation (51)) as the convection speed in the coplanarity plane. A similar derivation can be applied out of the coplanarity plane.

The steps for solution are quite similar to those described in Section D.1. In Equation (35) for the Fourier-transformed distribution function, we must also include the loss term, $\tilde{f}/\tau$. As before, for $x\neq 0$, we take $\tilde{f}\propto\exp(\alpha x)$, which leads to a quadratic equation that is solved upstream and downstream:

$$-\alpha^2\kappa_{xx}+\alpha\left(u_x-2ik\kappa_{xz}\right)+iku_z+k^2\kappa_{zz}+1/\tau=0.\quad(79)$$

Note the additional term $1/\tau$ that appears on the left-hand side. The solution for α_j is given by (where upstream applies for $j=1$ and downstream for $j=2$)

$$\alpha_j=\frac{u_{xj}}{2\kappa_{xxj}}-ik\frac{\kappa_{xzj}}{\kappa_{xxj}}+\frac{(-1)^{j+1}}{\kappa_{xxj}}\times\sqrt{u_{xj}^2/4+\kappa_{\|j}\kappa_{\perp j}k^2+ik\left(\kappa_{xxj}u_{zj}-\kappa_{xzj}u_{xj}\right)+\kappa_{xxj}/\tau}.\quad(80)$$

The solution for $\tilde{f}(k,p)$, and, in turn, the distribution function at the shock is

$$f_{\rm s}(z,p)=\frac{3Q_0}{2\pi\Delta up_{\rm inj}}\left(\frac{p}{p_{\rm inj}}\right)^{-3/2}\int_{-\infty}^{\infty}dk\,\exp\left(ikz-\frac{3}{\Delta u}\times\int_{\ln p_{\rm inj}}^{\ln p}d\ln p'\sum_{j=1}^{2}\sqrt{\frac{u_{xj}^2}{4}+\kappa_{\|j}\kappa_{\perp j}k^2+ik\left(\kappa_{xxj}u_{zj}-\kappa_{xzj}u_{xj}\right)+\kappa_{xxj}/\tau}\right).\quad(81)$$

Utilizing the previous expansions, we obtain the following separable solution:

$$f_s^{\rm loss}(z,p)=f_{\rm s}(z,p)g^{\rm loss}(p),\quad(82)$$

where $f_{\rm s}(z,p)$ is the solution previously obtained and $g^{\rm loss}(p)$ is a term characterizing the effects of loss:

$$g^{\rm loss}(p)=\exp\left(-\frac{3}{\Delta u}\int_{\ln p_{\rm inj}}^{\ln p}d\ln p'\times\sum_{j=1}^{2}\sqrt{\frac{u_{xj}^2}{4}+\frac{\kappa_{xxj}}{\tau\nu^{\chi+1}}\left(\nu'\right)^{\chi+1}}-\frac{u_{xj}}{2}\right)\quad(83)$$

$$\approx\exp\left(-\frac{3}{\Delta u}\int_{\ln p_{\rm inj}}^{\ln p}d\ln p'\sum_{j=1}^{2}\sqrt{\frac{\kappa_{xxj}}{\tau\nu^{\chi+1}}}\left(\nu'\right)^{(\chi+1)/2}\right)=\exp\left(-\frac{6}{(\chi+1)\Delta u}\sum_{j=1}^{2}\sqrt{\frac{\kappa_{xxj}}{\tau}}\left[1-\left(\frac{\nu_{\rm inj}}{\nu}\right)^{(\chi+1)/2}\right]\right)\quad(84)$$

where $\nu_{\rm inj}$ is the particle injection speed.

Because the solution $f_s^{\rm loss}(z,p)$ is separable, the term $g^{\rm loss}(p)$ is also carried through the total distribution function, $F_{\rm s}^{\rm loss}(z,p)$, integrated over the locus of injection points:

$$F_{\rm s}^{\rm loss}(z,p)=F_{\rm s}(z,p)g^{\rm loss}(p),\quad(85)$$

where $F_{\rm s}(z,p)$ is the previous total distribution with no loss effects (Equation (75)).

REFERENCES

Aschwanden, M. 2006, SSRv, 124, 361
Aulanier, G., Török, T., Démoulin, P., & DeLuca, E. E. 2010, ApJ, 708, 314
Battarbee, M., Laitinen, T., & Vainio, R. 2011, A&A, 535, A34
Battarbee, M., Vainio, R., Laitinen, T., & Hietala, H. 2013, A&A, 558, A110
Bell, A. R. 1978a, MNRAS, 182, 147
Bell, A. R. 1978b, MNRAS, 182, 443
Bisi, M. M., Breen, A. R., Jackson, B. V., et al. 2010, SoPh, 265, 49
Cucinotta, F. A., Hu, S., Schwadron, N. A., et al. 2010, SpWea, 8, 0
Dayeh, M. A., Desai, M. I., Dwyer, J. R., et al. 2009, ApJ, 693, 1588
Desai, M. I., Dayeh, M. A., Ebert, R. W., et al. 2015, ApJ, submitted
Dröge, W. 2005, AdSpR, 35, 532
Drury, L. O. 1983, RPPh, 46, 973
Fermi, E. 1949, PhRv, 75, 1169
Giacalone, J. 2001, in The Outer Heliosphere: The Next Frontiers, ed. K. Scherer et al. (Amsterdam: Pergamon Press), 377
Giacalone, J. 2005, ApJL, 628, L37
Giacalone, J., & Jokipii, J. R. 1999, ApJ, 520, 204
Giacalone, J., Jokipii, J. R., & Kóta, J. 2002, ApJ, 573, 845
Gopalswamy, N., Aguilar-Rodriguez, E., Yashiro, S., et al. 2005, JGRA, 110, 12
Gorby, M. J., Schwadron, N. A., Linker, J. A., et al. 2012, AGU Fall Meeting Abstracts (Washington, DC: AGU), A2216
Jokipii, J. R. 1982, ApJ, 255, 716
Jokipii, J. R. 1986, JGR, 91, 2929
Jokipii, J. R. 1987, ApJ, 313, 842
Jokipii, J. R., Giacalone, J., & Kota, J. 2003, in Proc. 28th ICRC, ed. T. Kajita et al. (Singapore: IUPAP), 3685
Jokipii, J. R., & Parker, E. N. 1969, ApJ, 155, 777
Kliem, B., & Török, T. 2006, PhRvL, 96, 255002
Kocharov, L., Lytova, M., Vainio, R., Laitinen, T., & Torsti, J. 2005, ApJ, 620, 1052
Kóta, J., Manchester, W. B., & Gombosi, T. I. 2005a, in Proc. 29th ICRC, ed. B. Sripathi et al. (Singapore: IUPAP), 125
Kóta, J., Manchester, W. B., Jokipii, J. R., de Zeeuw, D. L., & Gombosi, T. I. 2005b, in AIP Conf. Ser. 781, The Physics of Collisionless Shocks: 4th Annual IGPP International Astrophysics Conference, ed. G. Li, G. P. Zank & C. T. Russell (Melville, NY: AIP), 201
Kozarev, K. A., Evans, R. M., Schwadron, N. A., et al. 2013, ApJ, 778, 43
Kozarev, K. A., Korreck, K. E., Lobzin, V. V., Weber, M. A., & Schwadron, N. A. 2011, ApJL, 733, L25
Lee, M. A. 1983, JGR, 88, 6109
Lee, M. A. 2005, ApJS, 158, 38
Lee, M. A., Fisk, L. A., & Skadron, G. 1981, GeoRL, 8, 401

Li, G., Zank, G. P., Verkhoglyadova, O., et al. 2009, ApJ, 702, 998
Linker, J., Mikic, Z., Schwadron, N., et al. 2014, in COSPAR Meeting 40, 40th COSPAR Scientific Assembly, 1840
Linker, J. A., & Mikić, Z. 1997, in Coronal Mass Ejections, Vol. 99, ed. N. Crooker, J. Joselyn & J. Feynmann (Washington, DC: AGU), 269
Linker, J. A., Mikić, Z., Biesecker, D., et al. 1999, JGR, 104, 809
Linker, J. A., Mikić, Z., Biesecker, D. A., et al. 1999, JGR, 104, 9809
Lionello, R., Downs, C., Linker, J. A., et al. 2013, ApJ, 777, 76
Lionello, R., Linker, J. A., & Mikić, Z. 2009, ApJ, 690, 902
Lionello, R., Mikić, Z., & Linker, J. A. 1999, JCoPh, 152, 346
Liu, W., Nitta, N. V., Schrijver, C. J., Title, A. M., & Tarbell, T. D. 2010, ApJL, 723, L53
Lugaz, N., Downs, C., Shibata, K., et al. 2011, ApJ, 738, 127
Ma, S., Raymond, J. C., Golub, L., et al. 2011, ApJ, 738, 160
Manchester, W. B., IV, Gombosi, T. I., de Zeeuw, D. L., et al. 2005, ApJ, 622, 1225
Manchester, W. B., IV, Vourlidas, A., Tóth, G., et al. 2008, ApJ, 684, 1448
Mason, G. M., Wiedenbeck, M. E., Miller, J. A., et al. 2002, ApJ, 574, 1039
Mewaldt, R. A., Cohen, C. M. S., Labrador, A. W., et al. 2005a, JGRA, 110, 9
Mewaldt, R. A., Cohen, C. M. S., Mason, G. M., et al. 2005b, in AIP Conf. Ser. 781, The Physics of Collisionless Shocks: 4th Annual IGPP International Astrophysics Conference, ed. G. Li, G. P. Zank & C. T. Russell (Melville, NY: AIP), 227
Mewaldt, R. A., Looper, M. D., Cohen, C. M. S., et al. 2012, SSRv, 171, 97
Mikić, Z., & Linker, J. A. 1994, ApJ, 430, 898
Mikić, Z., Linker, J. A., Schnack, D. D., Lionello, R., & Tarditi, A. 1999, PhPl, 6, 2217
Reames, D. V. 2009a, ApJ, 706, 844
Reames, D. V. 2009b, ApJ, 693, 812
Riley, P., Linker, J. A., Lionello, R., & Mikic, Z. 2012, JASTP, 83, 1
Riley, P., & Lionello, R. 2011, SoPh, 270, 575
Roussev, I. I., Sokolov, I. V., Forbes, T. G., et al. 2004, ApJL, 605, L73
Schwadron, N. A., Blake, J. B., Case, A. W., et al. 2014, SpWea, 12, 622
Schwadron, N. A., Lee, M. A., & McComas, D. J. 2008, ApJ, 675, 1584
Schwadron, N. A., Townsend, L., Kozarev, K., et al. 2010, SpWea, 8, 0
Titov, V. S., & Démoulin, P. 1999, A&A, 351, 707
Titov, V. S., Török, T., Mikic, Z., & Linker, J. A. 2014, ApJ, 790, 163
Török, T., & Kliem, B. 2007, Astron. Notes, 328, 743
Török, T., Panasenco, O., Titov, V. S., et al. 2011, ApJL, 739, L63
Tsurutani, B., Wu, S. T., Zhang, T. X., & Dryer, M. 2003, A&A, 412, 293
Vainio, R., Pönni, A., Battarbee, M., et al. 2014, JSWSC, 4, A8
Verkhoglyadova, O. P., Li, G., Zank, G. P., & Hu, Q. 2008, in AIP Conf. Ser. 1039, Particle Acceleration and Transport in the Heliosphere and Beyond, ed. G. Li et al. (Melville, NY: AIP), 214
Veronig, A. M., Muhr, N., Kienreich, I. W., Temmer, M., & Vršnak, B. 2010, ApJL, 716, L57
Wang, Y., & Zhang, J. 2008, ApJ, 680, 1516
Zank, G. P., Li, G., Florinski, V., et al. 2006, JGRA, 111, 6108
Zhang, M., Qin, G., & Rassoul, H. 2009, ApJ, 692, 109